

pubs.acs.org/acschemicalbiology Articles

# Uncovering the Association Mechanism between Two Intrinsically Flexible Proteins

Angy Liseth Dávalos, José David Rivera Echeverri, Denize C. Favaro, Ronaldo Junio de Oliveira, Gustavo Penteado Battesini Carretero, Caroline Lacerda, Iolanda Midea Cuccovia, Marcus Vinicius Cangussu Cardoso, Chuck S. Farah, and Roberto Kopke Salinas\*



Cite This: ACS Chem. Biol. 2024, 19, 669-686



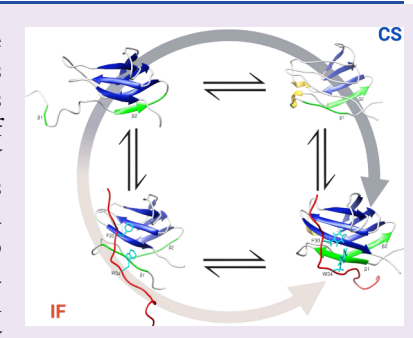
**ACCESS** 

Metrics & More

Article Recommendations

Supporting Information

ABSTRACT: The understanding of protein—protein interaction mechanisms is key to the atomistic description of cell signaling pathways and for the development of new drugs. In this context, the mechanism of intrinsically disordered proteins folding upon binding has attracted attention. The VirB9 C-terminal domain (VirB9<sup>Ct</sup>) and the VirB7 N-terminal motif (VirB7<sup>Nt</sup>) associate with VirB10 to form the outer membrane core complex of the Type IV Secretion System injectisome. Despite forming a stable and rigid complex, VirB7<sup>Nt</sup> behaves as a random coil, while VirB9<sup>Ct</sup> is intrinsically dynamic in the free state. Here we combined NMR, stopped-flow fluorescence, and computer simulations using structure-based models to characterize the VirB9<sup>Ct</sup>-VirB7<sup>Nt</sup> coupled folding and binding mechanism. Qualitative data analysis suggested that VirB9<sup>Ct</sup> preferentially binds to VirB7<sup>Nt</sup> by way of a conformational selection mechanism at lower temperatures. However, at higher temperatures, energy



barriers between different VirB9<sup>Ct</sup> conformations are more easily surpassed. Under these conditions the formation of non-native initial encounter complexes may provide alternative pathways toward the native complex conformation. These observations highlight the intimate relationship between folding and binding, calling attention to the fact that the two molecular partners must search for the most favored intramolecular and intermolecular interactions on a rugged and funnelled conformational energy landscape, along which multiple intermediates may lead to the final native state.

#### INTRODUCTION

Intrinsically disordered proteins (IDPs) are fully functional despite lacking a defined folded structure. When combined with folded domains, they are called intrinsically disordered regions (IDRs). <sup>1-4</sup> IDPs/IDRs may be classified as molecular recognition features (MoRFs), short linear motifs (SLiMs), or low-complexity regions (LCRs). While fuzzy complexes retaining a high degree of disorder in the bound state have been described, <sup>6-9</sup> most MoRFs become structured upon binding to well-folded partners.

The understanding of protein—protein interaction mechanisms is key to the atomic level description of cell signaling pathways and for the development of new drugs. In this context, the mechanism of IDPs/IDRs folding upon binding is of significant interest. The induced-fit and conformational selection mechanisms have been widely used to explain protein—ligand interactions. In the context of IDPs/IDRs, the conformational selection mechanism requires unfolded and folded or partially folded conformations to be in equilibrium with each other, with one of them being the binding competent conformation. In contrast, the induced fit mechanism requires that folding occurs after binding. Folding and binding have been considered as analogous processes, which may be interpreted in the framework of folding funnels. Is—20 The rugged conformational energy landscape of IDPs/IDRs

binding equilibrium could provide multiple pathways for the system to progress downhill toward the native complex. Consistent with this view, it was predicted that induced-fit and conformational selection could coexist, and the relative importance of one or the other mechanism could be regulated by the ligand concentration. Indeed, complex mixtures of induced-fit and conformational selection have been described. Ar, 19,10,22 In addition, the formation of productive initial encounter complexes between IDPs and folded proteins has been observed by NMR. Therefore, folding coupled to binding seems to be a highly cooperative process with few short-lived intermediates, resembling the folding of globular proteins. Es

Bacteria use secretion systems or injectisomes to transport macromolecules, such as proteins or DNA, across the bacterial cell envelope and to inject them into another prokaryotic or eukaryotic cell.<sup>26</sup> Among them, the Type IV Secretion System from the phytopathogen *Xanthomonas citri* (X-T4SS) is

Received: October 24, 2023 Revised: February 1, 2024 Accepted: February 7, 2024 Published: March 5, 2024





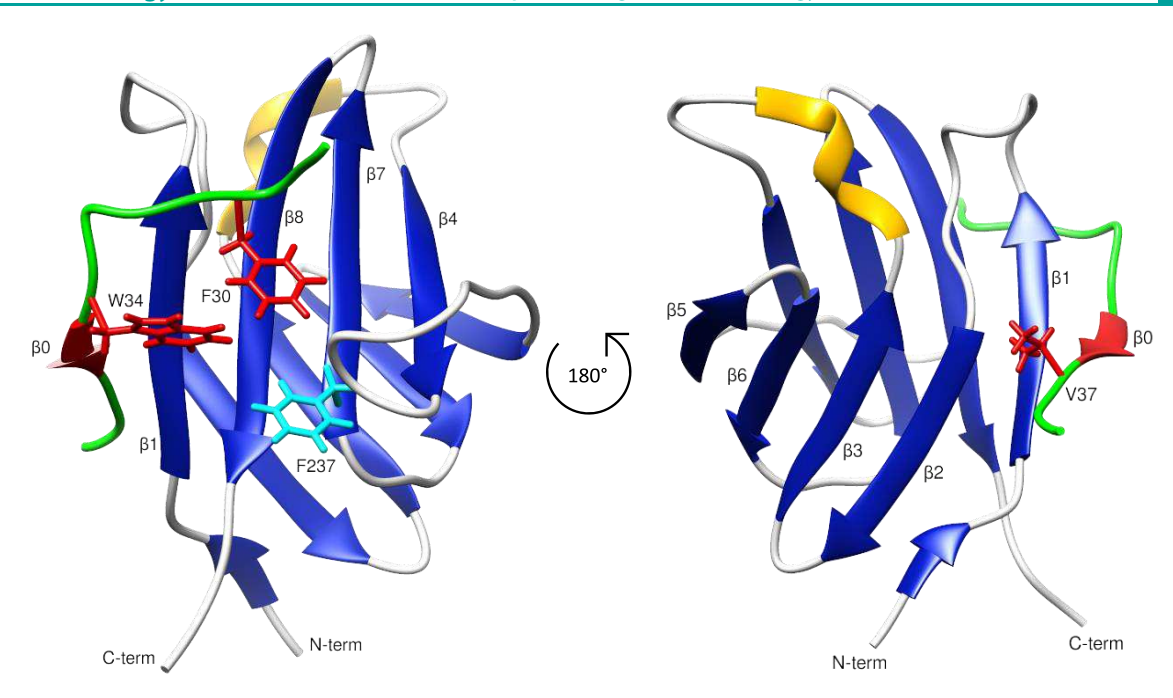


**Figure 1.** NMR solution structure of the VirB9<sup>Ct</sup> – VirB7<sup>Nt</sup> complex (PDB 2N01). The secondary structure is color-coded blue for  $\beta$ -strand and yellow for helix. VirB7<sup>Nt</sup> is shown in green and the VirB7<sup>Nt</sup>  $\beta$ 0 is shown in red. VirB7<sup>Nt</sup> side chain residues F30 and W34 are shown in sticks and red-colored, while VirB9<sup>Ct</sup> F237 side chain is shown in cyan. This complex is stabilized by a series of interactions between VirB7<sup>Nt</sup> aromatic residues, F30 and W34, and VirB9<sup>Ct</sup> solvent exposed side chains on the surface of the  $\beta$ 1- $\beta$ 8- $\beta$ 7- $\beta$ 4  $\beta$ -sheet, and by the accommodation of VirB7<sup>Nt</sup> V37 in a hydrophobic cleft formed between VirB9<sup>Ct</sup> strands  $\beta$ 1 and  $\beta$ 2.

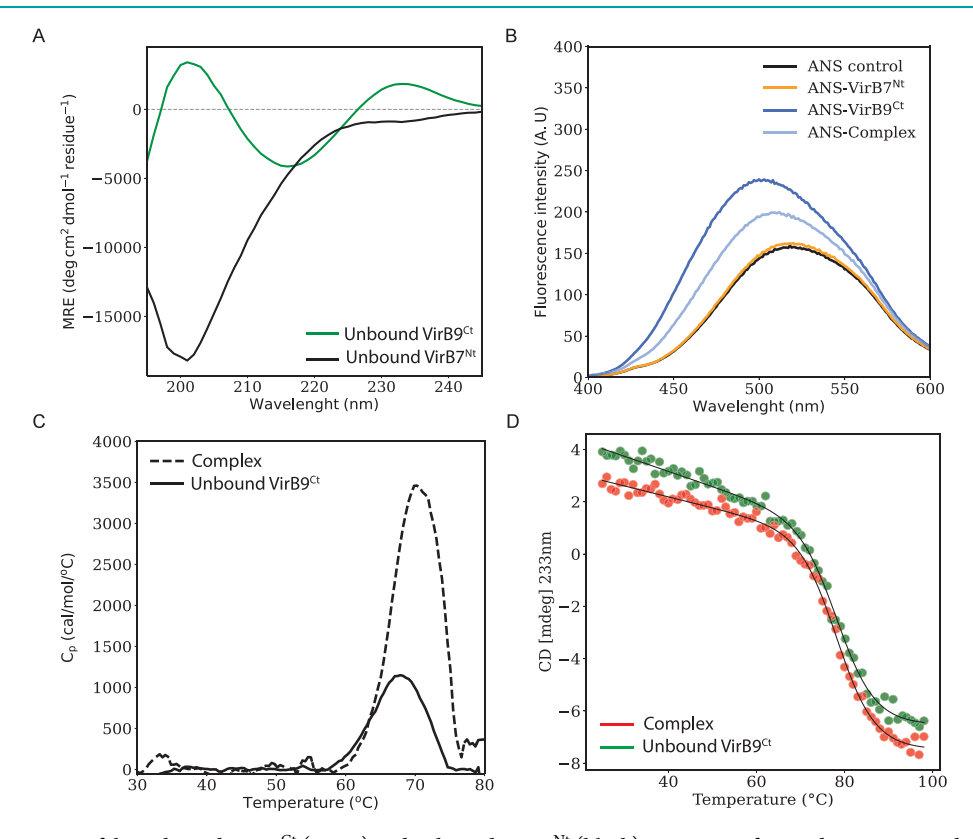


Figure 2. Far-UV CD spectra of the unbound VirB9<sup>Ct</sup> (green) and unbound VirB7<sup>Nt</sup> (black). Fractions of secondary structure obtained by quantitative CD spectral analysis: 37 and 21% of β-type, 0 and 0.04% of helix, 26 and 16% of turns and 36 and 58% of unordered conformations for the unbound VirB9<sup>Ct</sup> and the unbound VirB7<sup>Nt</sup>, respectively (A). ANS fluorescence spectra recorded in the working buffer (control) or in the presence of VirB7<sup>Nt</sup>, VirB9<sup>Ct</sup>, or the VirB7<sup>Nt</sup>–VirB9<sup>Ct</sup> complex (B). Thermal denaturation of the unbound VirB9<sup>Ct</sup> and of the VirB7<sup>Nt</sup>–VirB9<sup>Ct</sup> complex monitored by DSC (C) or CD at 233 nm (D).

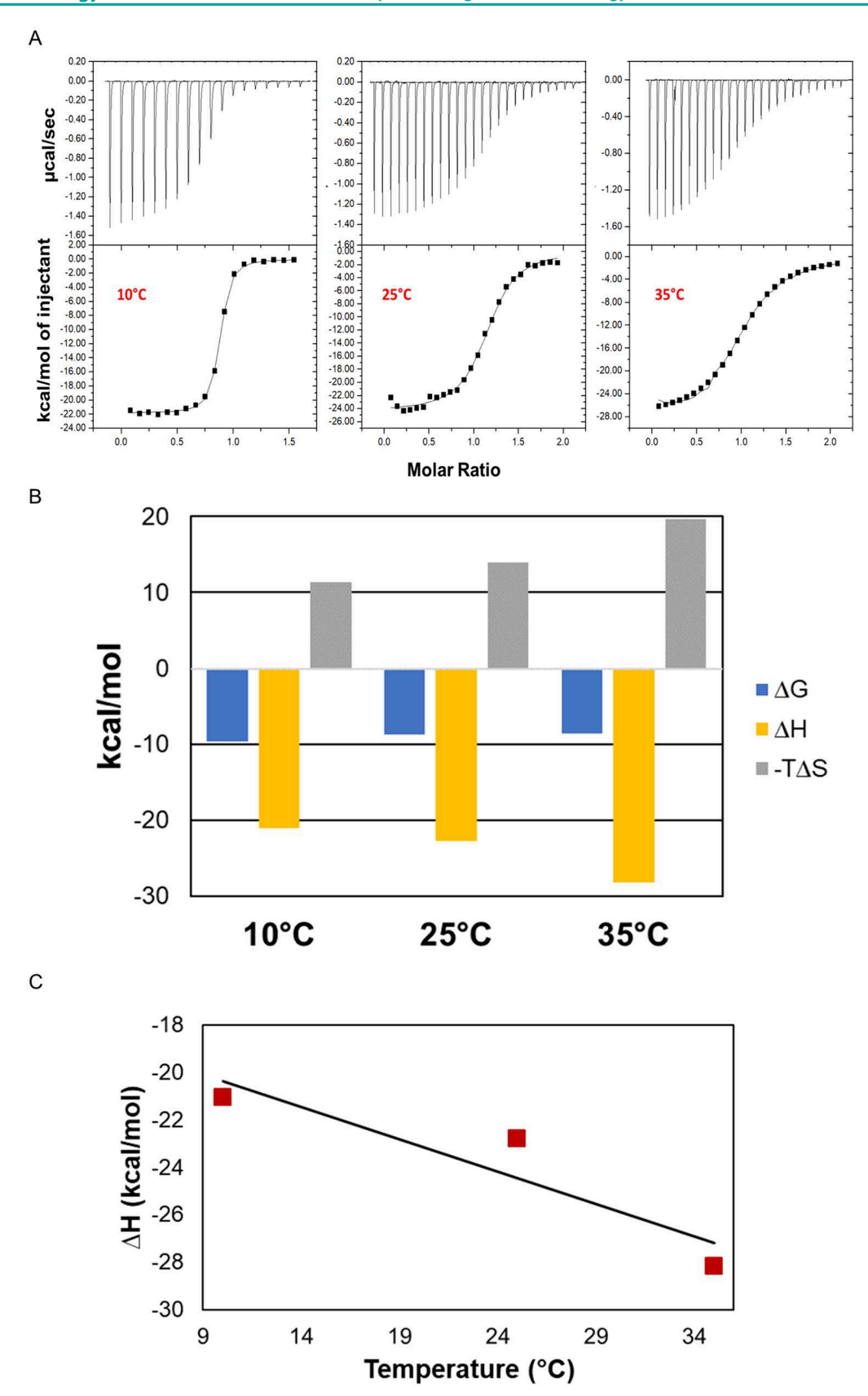
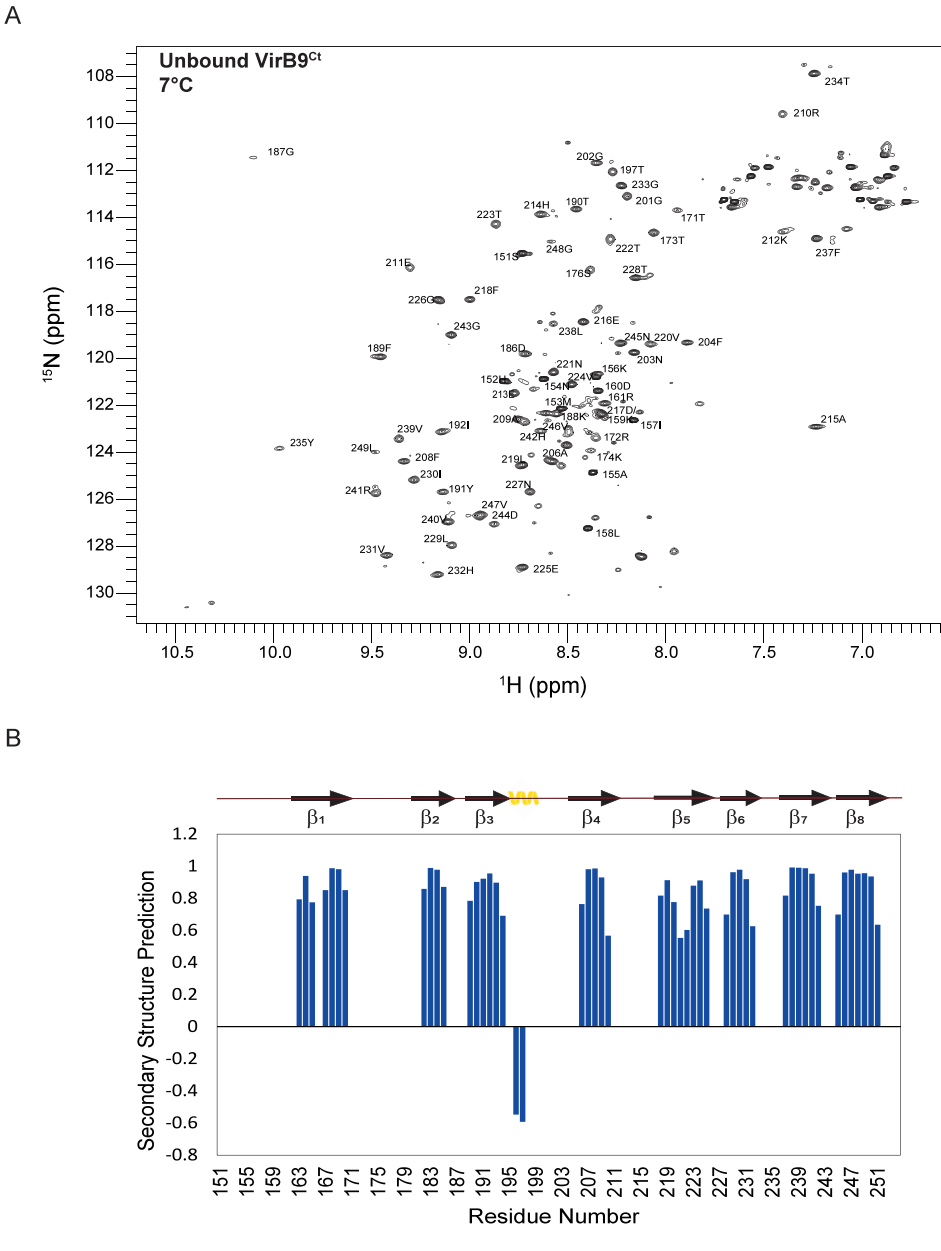


Figure 3. Isothermal titration calorymetry (ITC) thermograms of VirB7<sup>Nt</sup> being titrated with VirB9<sup>Ct</sup> at 10, 25, and 35 °C (A). Values of  $\Delta H^0$ ,  $-T \times \Delta S^0$ , and  $\Delta G^0$  obtained from fitting the ITC data to a 1:1 stoichiometric model (B).  $\Delta C_p$  (-0.23 kcal/(mol  $\times$  K)) obtained from the slope of the graph of  $\Delta H^0$  as a function of temperature (C).



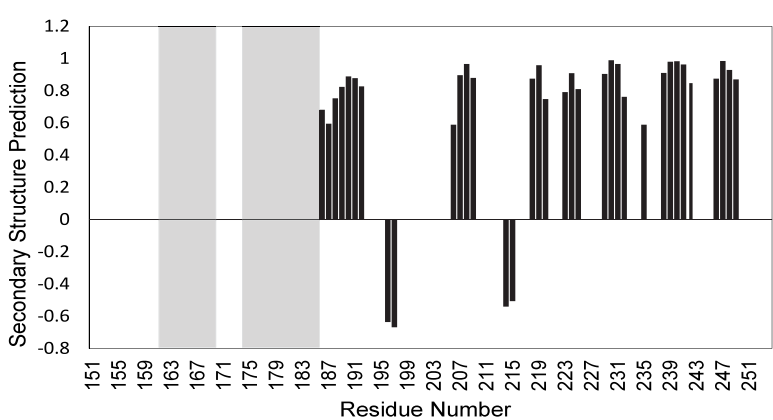


Figure 4. Assignment of the unbound VirB9<sup>Ct1</sup>H $^{-15}$ N HSQC spectrum at 7 °C (A). TALOS<sup>+</sup> secondary structure prediction for the bound (blue) and the unbound (black) states of VirB9<sup>Ct</sup> at 35 and 7 °C, respectively. Unassigned residues are highlighted by gray-colored rectangles (B).

specialized in the secretion of toxins that kill other Gramnegative bacteria. <sup>27</sup> The X-T4SS is part of the warfare arsenal

that enables X. citri to compete for space and resources with other bacteria.  $^{27,28}$  Structural characterization of the X-T4SS

outer membrane core complex (OMCC) showed a tetradecameric ring formed by multiple copies of VirB7, VirB9, and VirB10. This large assembly spans the bacterial periplasm, making a pore in the outer membrane. The VirB7–VirB9 interaction is stabilized by the binding of VirB7 N-terminal tail (VirB7<sup>Nt</sup>) to the VirB9 C-terminal domain (VirB9<sup>Ct</sup>). This VirB7<sup>Nt</sup>–VirB9<sup>Ct</sup> complex consists of a sandwich of two antiparallel  $\beta$ -sheets, one of them formed by four VirB9<sup>Ct</sup>  $\beta$ -strands, and another formed by a short VirB7  $\beta$ -strand that pairs with VirB9  $\beta$ 1, forming the  $\beta$ 0– $\beta$ 1– $\beta$ 8– $\beta$ 7– $\beta$ 4  $\beta$ -sheet (Figure 1). <sup>28,29</sup> The VirB7<sup>Nt</sup>–VirB9<sup>Ct</sup> interaction was shown to be critical for OMCC stabilization and X-T4SS functioning. <sup>29</sup>

NMR data indicated that VirB7<sup>Nt</sup> is intrinsically disordered in the absence of VirB9<sup>Ct</sup>, while the latter is highly flexible, presumably a molten globule, in the free state. <sup>29,30</sup> Considering their intrinsic dynamic nature, VirB9<sup>Ct</sup> and VirB7<sup>Nt</sup> form an ideal model system to study the mechanism of coupled folding and binding between two intrinsically flexible proteins. To this end, we characterized the VirB7<sup>Nt</sup>–VirB9<sup>Ct</sup> binding mechanism using a combination of <sup>15</sup>N chemical exchange saturation transfer (CEST) experiments, stopped-flow fluorescence and computer simulations using classical and structure-based models.

## ■ RESULTS AND DISCUSSION

Structural Characterization of VirB9<sup>Ct</sup> in the Unbound **State.** The circular dichroism (CD) spectrum of VirB9<sup>Ct</sup> in aqueous solution showed a negative band at 218 nm indicative of  $\beta$ -type structures (Figure 2A).<sup>31</sup> A quantitative analysis of this spectrum indicated that approximately 39 VirB9<sup>Ct</sup> residues (37%) are in the  $\beta$ -type conformation. The NMR structure of the VirB7<sup>Nt</sup>-VirB9<sup>Ct</sup> complex (PDB 2N01) showed a slightly larger number of residues, 46 VirB9<sup>Ct</sup> residues (44%), in  $\beta$ -type conformation.<sup>29</sup> The positive CD band at 232–233 nm could be due to the presence of six phenylalanines and one tryptophan in the VirB9<sup>Ct</sup> amino acid sequence. It is known that aromatic residues may give rise to exciton coupling effects, 32-35 which seem to significantly contribute to the CD spectra of proteins with low helical content.<sup>32</sup> The CD spectrum of VirB7<sup>Nt</sup> is typical of a random coil, as expected for a short peptide in aqueous solution (Figure 2A). The VirB7<sup>Nt</sup> peptide is a good model for the N-terminal tail within VirB7, which shows fast backbone motions, as revealed by measurements of 15N relaxation rates.30

The hydrophobic fluorescent probe 8-anilino-1-naphthalene sulfonic acid (ANS) is a good probe of solvent-exposed hydrophobic surface patches on proteins. Binding of ANS to hydrophobic patches is accompanied by an increase in fluorescence intensity and a shift of the fluorescence spectrum toward shorter wavelengths. Addition of VirB7Nt did not affect the ANS fluorescence (Figure 2B). However, the addition of either VirB9Ct alone or in complex with VirB7Nt resulted in a small but significant increase in the ANS fluorescence accompanied by a blue-shift of the spectrum (Figure 2B). The greater ANS fluorescence change observed upon addition of the free protein relative to the complex indicates that the unbound VirB9Ct exposes a greater amount of hydrophobic surface area than the complex.

The thermal denaturation of VirB9<sup>Ct</sup> and of the VirB9<sup>Ct</sup>–VirB7<sup>Nt</sup> complex was monitored by differential scanning calorimetry ( $\mu$ -DSC) and CD. A reversible thermal transition was observed at nearly the same melting temperature ( $T_{\rm m}$ ) for the unbound VirB9<sup>Ct</sup> and for the complex by both methods (Figure 2C,D). This observation was surprising since binding to

VirB7<sup>Nt</sup> was expected to promote an extra thermal stabilization of VirB9<sup>Ct</sup>, which should be reflected in a higher  $T_{\rm m}$  relative to the unbound protein. Notably, the thermal denaturation experiment showed that the complex has significantly higher unfolding enthalpy (29.57 kcal/mol) than the unbound VirB9<sup>Ct</sup> (10.42 kcal/mol; Figure 2C). This observation may be explained considering that VirB9<sup>Ct</sup>–VirB7<sup>Nt</sup> unfolding and dissociation occur within a single transition as a consequence of the coupling between these two processes.

The magnitude of the heat capacity change upon binding  $(\Delta C_{\rm p})$  is strongly correlated to the amount of solvent-exposed surface area that is buried upon complex formation.  $^{45-47}$  Binding of VirB9 $^{\rm Ct}$  to VirB7 $^{\rm Nt}$  is enthalpically driven as indicated by isothermal titration calorimetry (ITC) experiments carried out at 10, 25, and 35 °C (Figure 3A,B). The VirB9 $^{\rm Ct}$ –VirB7 $^{\rm Nt}$   $K_{\rm d}^{\rm app}$  (see Experimental Section) is 0.70  $\mu{\rm M}$  at 35 °C, similar to the value reported before. Analysis of the binding  $\Delta H$  temperature dependence revealed a  $\Delta C_{\rm p}=-0.23$  kcal/(mol  $\times$  K) (Figure 3C), which is a small value consistent with an interaction with minor conformational rearrangements. Analysis an example, binding of the HIV-1 envelope glycoprotein gp120 to the human cell surface CD4 receptor involves substantial structuring coupled to binding, which is reflected on a large  $\Delta C_{\rm p}=-1.30$  kcal/(mol  $\times$  K). In contrast, binding of mAb b12 to gp120 does not induce any conformational structuring and leads to a reduced  $\Delta C_{\rm p}=-0.40$  kcal/(mol  $\times$  K).

We used solution NMR spectroscopy to characterize the structure of VirB9<sup>Ct</sup> in the unbound state. The <sup>1</sup>H-<sup>15</sup>N HSQC spectrum of the unbound protein showed a lower number of cross-peaks than expected based on the amino acid sequence. However, the NMR spectrum quality improved significantly when the temperature was decreased from 35 to 7 °C (Supporting Information, Figure S1). From the 100 <sup>1</sup>H-<sup>15</sup>N cross peaks expected based on the VirB9<sup>Ct</sup> amino acid sequence, approximately 92 were detected at 7 °C. We successfully assigned 70 of them from the analysis of a set of multidimensional triple resonance NMR experiments recorded at the lowest possible temperature (Figure 4A). The unassigned residues were mainly located within  $\beta$ -strands  $\beta 1$  and  $\beta 2$ , which form the VirB7<sup>Nt</sup> binding site (Figure 1). Secondary structure prediction based on the assigned chemical shifts using TALOS<sup>+50</sup> indicated that  $\beta$  strands  $\beta_3$  to  $\beta_8$  were already folded in the unbound state, as well as the short  $3_{10}$ -helix in the  $\beta_3$ - $\beta_4$  interstrand loop (Figure 4B). Curiously, an additional short  $\alpha$ -helix was detected in the  $\beta_4$ - $\beta_5$  interstrand loop (Figure 4B). This extra helix is absent in the structure of the bound state, however, the NMR structure of the complex was solved at a significantly higher temperature, 35 °C (Figure 1).<sup>29</sup>

To obtain additional chemical shift information for the unbound VirB9<sup>Ct</sup>, particularly along  $\beta$ -strands  $\beta$ 1 and  $\beta$ 2, we performed chemical exchange saturation transfer (CEST) experiments of <sup>15</sup>N-labeled VirB9<sup>Ct</sup> in the presence of substoichiometric concentrations of unlabeled VirB7<sup>Nt</sup>. This <sup>15</sup>N-CEST experiment was recorded at 35 °C instead of 7 °C because the exchange between unbound and bound VirB9<sup>Ct</sup> was not observed at lower temperatures (Supporting Information, Figure S2). This observation is probably a consequence of the increased affinity between VirB9<sup>Ct</sup> and VirB7<sup>Nt</sup> at low temperatures as indicated by ITC. The binding free energy decreased slightly from  $\Delta G = -8.58$  kcal × mol<sup>-1</sup> at 35 °C to -8.76 kcal × mol<sup>-1</sup> at 25 °C (Figure 3). Such small change in free energy leads to almost two times greater affinity at 25 °C compared to 35 °C. Analysis of the <sup>15</sup>N-CEST experiment

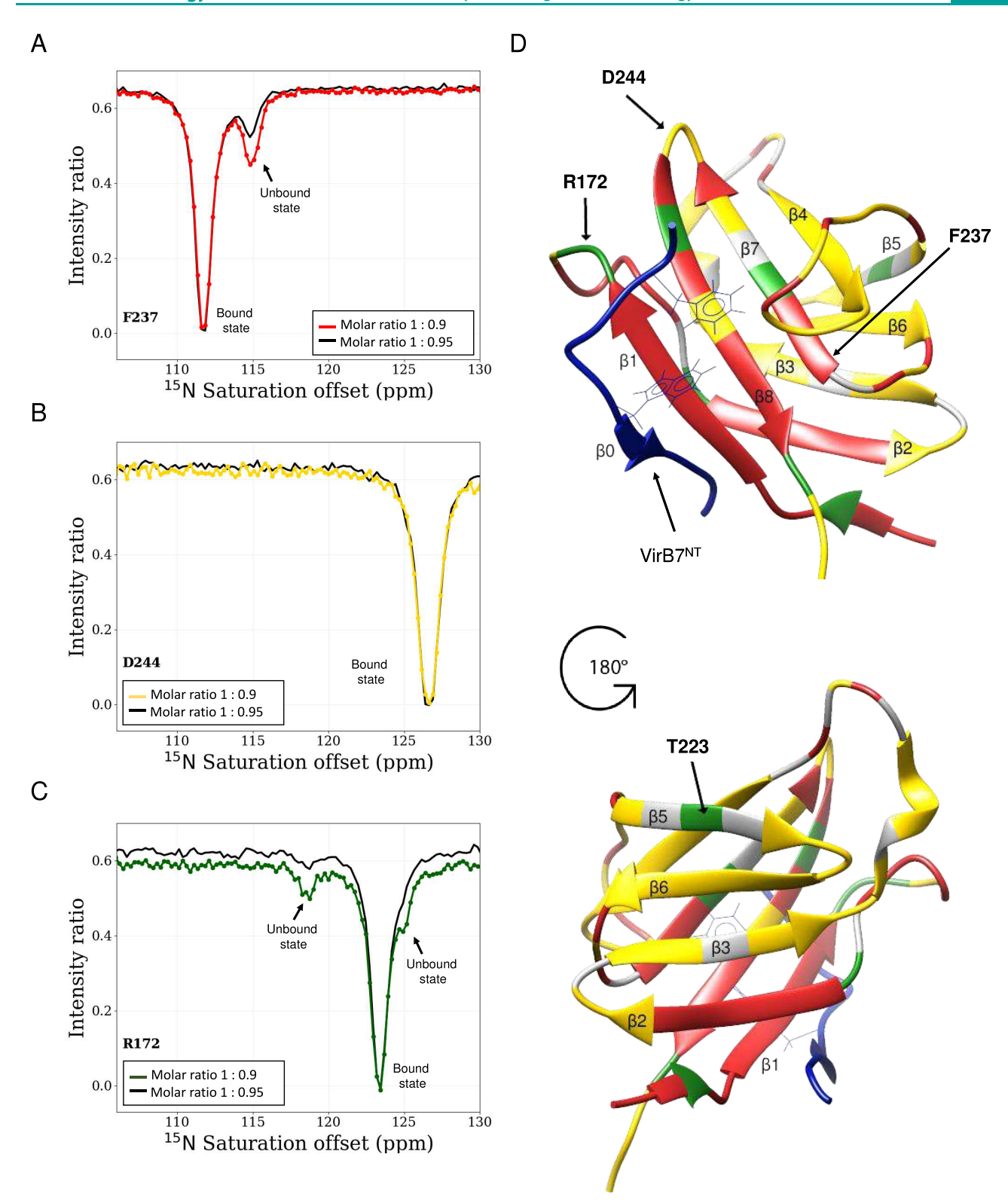
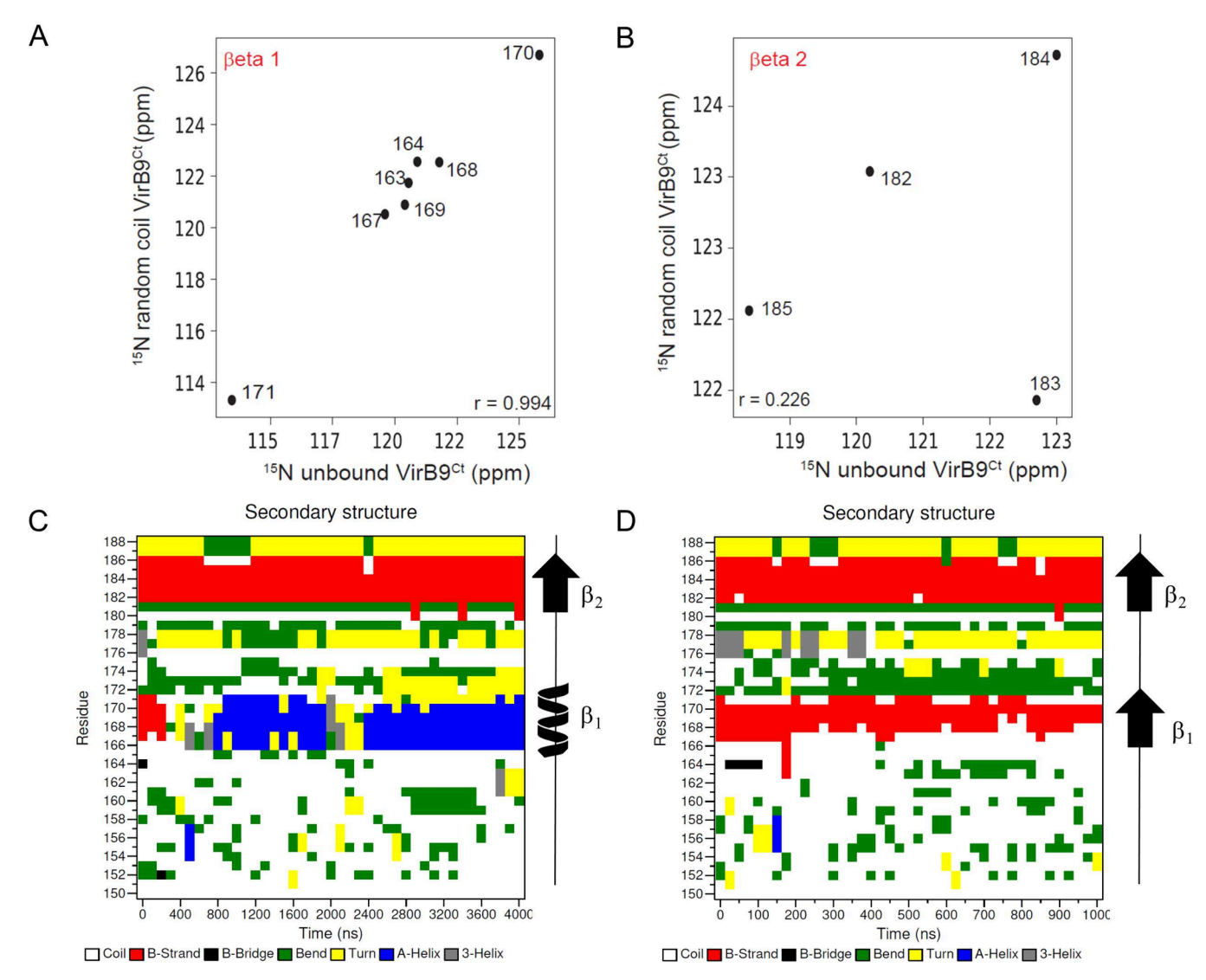


Figure 5. Representative <sup>15</sup>N CEST profiles obtained with samples of VirB9<sup>Ct</sup>-VirB7<sup>Nt</sup> at approximately 1:0.9 (colored) and 1:0.95 (black) (VirB9<sup>Ct</sup>:VirB7<sup>Nt</sup>) molar ratios for residues F237 (A), D244 (B), and R172 (C). VirB9<sup>Ct</sup> residues displaying <sup>15</sup>N-CEST profiles according to A (two CEST dips), B (one CEST dip), and C (three or more CEST dips) are color-coded red, yellow, and green, respectively, on the structure of the complex (D). The VirB7<sup>Nt</sup> peptide is shown in blue.

showed that some of the VirB9<sup>Ct</sup> residues presented two <sup>15</sup>N-CEST dips as exemplified by F237 in  $\beta$ 7 (Figure 5A), revealing a two-states chemical exchange process, while others, exemplified by D244 in the  $\beta$ 7– $\beta$ 8 interstrand loop, showed only a single

<sup>15</sup>N-CEST dip and no evidence of chemical exchange at all (Figure 5B). Furthermore, a subset of residues such as R172 in the  $\beta$ 1- $\beta$ 2 interstrand loop, displayed three <sup>15</sup>N-CEST dips reveling a three-states exchange process (Figure 5C). Further



**Figure 6.** Comparison between the experimental backbone <sup>15</sup>N chemical shifts obtained for VirB9<sup>Ct</sup> in the unbound state with the random coil <sup>15</sup>N chemical shifts predicted from the amino acid sequence. Only residues located at the  $\beta_1$  (A) and the  $\beta_2$  (B) were analyzed. Per-residue secondary structure of VirB9<sup>Ct</sup> in the VirB7<sup>Nt</sup>-unbound (C) and in the bound (D) states as a function of the simulation time. The dominant topology is shown on the right side.

addition of VirB7Nt caused a decrease in the magnitude of the smaller dips, corroborating their assignment to unbound VirB9<sup>Ct</sup> species in slow exchange with the major VirB7<sup>Nt</sup>-bound state (Figure 5A,C). All VirB9<sup>Ct</sup> residues that showed exchange between the unbound and the VirB7Nt-bound states were located within  $\beta$ -strands  $\beta 1$  and  $\beta 2$  or within the  $\beta 1 - \beta 7 - \beta 8 - \beta 4$ antiparallel  $\beta$ -sheet over which VirB7<sup>Nt</sup> lies on (residues colored red and green in Figure 5D). The single exception is T223 in  $\beta$ 5. The <sup>15</sup>N-CEST profiles displaying two-states exchange were fitted to the Bloch-McConnell equation assuming a two-state exchange model (Supporting Information, Figure S3). The fitted exchange rate was  $k_{\rm ex}^{\rm b} \approx 15-20~{\rm s}^{-1}$ , with the unbound state population  $p_{\rm A} \approx 7-10\%$  of the total VirB9<sup>Ct</sup> population. Backbone <sup>15</sup>N chemical shifts for residues located within VirB9<sup>Ct</sup>  $\beta$ 1 and  $\beta$ 2 in the unbound state were obtained from the analysis of the <sup>15</sup>N-CEST experiment (Supporting Information, Figure S4). The backbone <sup>15</sup>N chemical shifts for residues 163–171 along the  $\beta$ 1 showed a very good agreement with random coil chemical shifts predicted from the VirB9<sup>Ct</sup> amino acid sequence using the *ncIDP* online server, <sup>51</sup> while a poorer agreement was

observed along  $\beta 2$  (Figure 6A,B), suggesting that the VirB9<sup>Ct</sup>  $\beta 1$  is disordered in the absence of VirB7<sup>Nt</sup>. The relative instability of  $\beta 1$  is supported by molecular dynamics (MD) simulations of VirB9<sup>Ct</sup> in the unbound and in the VirB7<sup>Nt</sup>-bound states (Supporting Information, Figures S5 and S6). The simulations showed that  $\beta 1$  unfolded after approximately 300 ns in the absence of VirB7<sup>Nt</sup>, after which the corresponding region exchanged between disordered and helical conformations (Figure 6C and Supporting Information, Figure S5). In contrast, the same  $\beta$ -strand remained stable during the whole MD trajectory of the VirB7<sup>Nt</sup>-bound state (Figure 6D and Supporting Information, Figure S5).

Altogether we may conclude that the unbound VirB9<sup>Ct</sup> is almost fully folded except for  $\beta$ 1, which is disordered. Folding of a small  $\beta$ -strand rather than a larger conformational change is supported by the observation of a relatively small  $\Delta C_p$  due to VirB7<sup>Nt</sup>-binding (Figure 3) and by the CD spectrum that was consistent with all but one  $\beta$ -strand already folded in the unbound state (Figure 2). Indeed, the number of VirB9<sup>Ct</sup> residues in  $\beta$ -type conformation in the unbound state (predicted

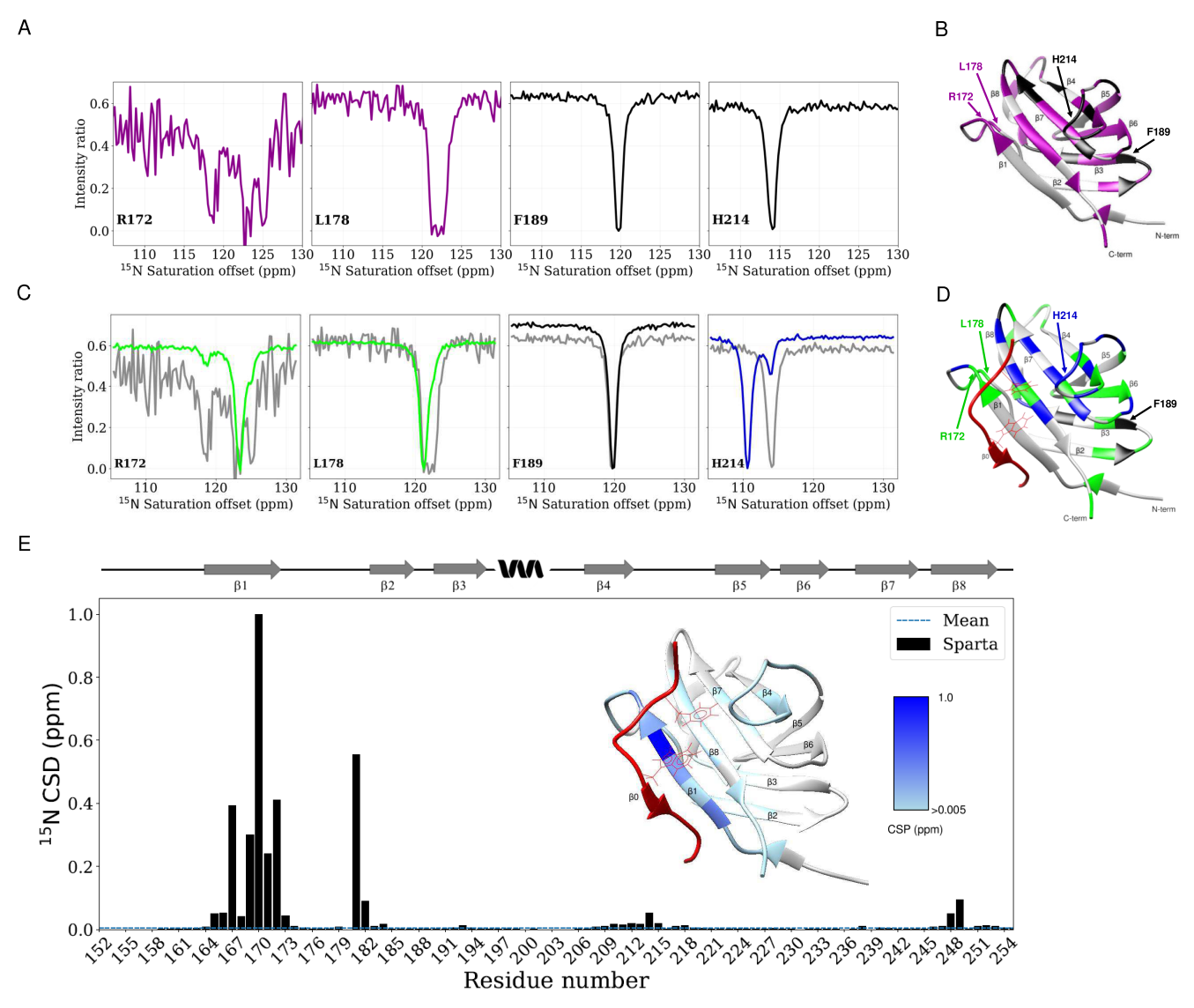


Figure 7. <sup>15</sup>N-CEST experiment recorded with VirB9<sup>Ct</sup> in the absence of VirB7<sup>Nt</sup>. Residues that showed multiple or broadened CEST dips suggestive of dynamics are color-coded magenta, while those that did not are color-coded black (A). VirB9<sup>Ct</sup> residues displaying <sup>15</sup>N-CEST profiles according to R172 and L178, and F189 and H214 are color-coded magenta and black, respectively, on the structure of the complex (B). Comparison between the <sup>15</sup>N-CEST experiments recorded in the presence (colored) and absence (gray) of VirB7<sup>Nt</sup> (C). Mapping of VirB9<sup>Ct</sup> residues on the structure of the complex according to (C). VirB9<sup>Ct</sup> Residues that showed significant <sup>15</sup>N chemical shift change upon binding to VirB7<sup>Nt</sup> are shown in blue, while those that experienced no chemical shift change at all are colored black. Residues displaying the bound-like conformation in the absence of VirB7<sup>Nt</sup> are color-coded green. VirB7<sup>Nt</sup> is shown in red (D). <sup>15</sup>N chemical shift difference (CSD) between VirB9<sup>Ct</sup> in the bound conformation in the presence and absence of VirB7<sup>Nt</sup>. The <sup>15</sup>N chemical shifts for the bound state came from the BMRB entry 25512.<sup>29</sup> The chemical shifts for the unbound state were predicted with Sparta<sup>52</sup> using the best model of the bound-state NMR structure (PDB 2N01) as input and the VirB7<sup>Nt</sup> coordinates deleted. The inset shows the CSD values color-coded on the VirB9<sup>Ct</sup>-VirB7<sup>Nt</sup> NMR structure (PDB 2N01). The VirB9<sup>Ct</sup> topology in complex is shown above and the VirB7<sup>Nt</sup> peptide is shown in red (E).

by CD) versus the VirB7<sup>Nt</sup>-bound state (computed from the NMR structure) differ by only 7, which is exactly the number of residues forming the  $\beta$ 1 strand.

VirB9<sup>Ct</sup> Samples the Bound Conformation in the Absence of VirB7<sup>Nt</sup>. Analysis of the <sup>15</sup>N-CEST experiment indicated that VirB9<sup>Ct</sup> assumes at least two unbound conformations in slow exchange equilibrium with the VirB7<sup>Nt</sup> bound state (Figure 5). As an attempt to test whether VirB7<sup>Nt</sup> would bind to one of the unbound VirB9<sup>Ct</sup> conformations rather than the other, we added a larger amount of VirB7<sup>Nt</sup> to the substoichiometric VirB9<sup>Ct</sup>-VirB7<sup>Nt</sup> sample and repeated the <sup>15</sup>N-CEST experiment. We observed a decrease in the magnitude of all CEST dips assigned to the unbound VirB9<sup>Ct</sup>

conformations (Figure 5C), indicating that VirB7<sup>Nt</sup> displays no preference toward a specific unbound VirB9<sup>Ct</sup> conformation or that the preferential binding to one of them rapidly shifts the equilibrium between the unbound conformations leading to a concomitant reduction in their populations.

We then investigated whether VirB9<sup>Ct</sup> could sample the bound conformation in the unbound state. To test this hypothesis, we compared  $^{15}{\rm N}$  CEST experiments recorded in the absence and presence of substoichiometric VirB7<sup>Nt</sup> concentrations at 35 °C (Figure 7A,C). Partial assignments for the unbound VirB9<sup>Ct 1</sup>H $^{-15}{\rm N}$  HSQC spectrum at 35 °C were obtained from the analysis of a  $^{15}{\rm N}_z$ -exchange experiment and a series of HSQC experiments recorded at increasing temper-

atures from 7 to 35 °C (Supporting Information, Figures S1 and S7). Some of the VirB9<sup>Ct</sup> residues exhibited a broad and rather noisy 15N-CEST profile in the unbound state, as shown for R172, while others exhibited well separated <sup>15</sup>N-CEST dips, indicating their engagement in the slow exchange equilibrium between distinct conformations, as shown for L178 in the  $\beta 1-\beta 2$  interstrand loop (Figure 7A,B). These observations revealed the dynamic regions of the unbound VirB9<sup>Ct</sup> (colored magenta in Figure 7B). Other residues, such as F189 and H214, showed a single CEST dip indicating that they were located in rigid parts of the unbound VirB9<sup>Ct</sup> (colored black in Figure 7A,B). The <sup>15</sup>N-CEST profiles for all residues located in the dynamic regions of the unbound state showed a drastic change upon the addition of VirB7Nt. Specifically, CEST dips corresponding to unbound conformations sharpened, giving rise to a major CEST dip at the bound state <sup>15</sup>N chemical shift as exemplified for R172 and L178 in the  $\beta 1-\beta 2$  interstrand loop (Figure 7C). These VirB9<sup>Ct</sup> residues (colored green in Figure 7D and Supporting Information, Figures S8 and S9) experience multiple conformations in the unbound state, one of them corresponding to the VirB7Nt-bound conformation. Residues located in the rigid parts of the unbound VirB9<sup>Ct</sup>, such as H214 and F189, exhibited a new 15N CEST dip corresponding to the VirB7<sup>Nt</sup>-bound state (H214) or experienced no change at all (F189) (Figure 7C,D). The latter cases, exemplified by F189, correspond to residues located far away from VirB7Nt binding site, explaining why they do not experience significant chemical shift changes upon VirB7<sup>Nt</sup> binding (Figure 7C,D, Supporting Information, Figure S11). The former cases, exemplified by H214, correspond to residues that experienced a significant <sup>15</sup>N chemical shift change upon binding (Figure 7D and Supporting Information, Figure S10). We used Sparta<sup>52</sup> to predict the VirB7<sup>Nt</sup> contribution to the VirB9<sup>Ct 15</sup>N chemical shift changes upon binding (Figure 7E). We observed that residues showing measurable <sup>15</sup>N chemical shift change were either located in regions where Sparta did predict some effect of the peptide (T173, K212, H214, A215, F218, L249) or in their vicinity (V247, N245, F237, V239, V220; Supporting Information, Figure S10 and Figure 7E). Therefore, such chemical shift perturbations seem to be explained by the dominant contribution of VirB7<sup>Nt</sup> binding over VirB9<sup>Ct</sup> conformation (Figure 7D,E). The observation of bound-like chemical shifts is consistent with conformational selection as a possible binding mechanism, which, however, does not exclude the occurrence of

alternative binding pathways.

VirB9<sup>Ct</sup>-VirB7<sup>Nt</sup> Binding Mechanism. The presence of tryptophan residues at positions 177 and 34 in VirB9<sup>Ct</sup> and VirB7<sup>Nt</sup>, respectively, and the millisecond exchange time scale between unbound and bound VirB9<sup>Ct</sup> states, favored the use of stopped-flow fluorescence to follow the VirB9<sup>Ct</sup>-VirB7<sup>Nt</sup> association kinetics. The analysis of the observed rate constants as a function of excess of ligand or protein concentration (pseudo and reverse-pseudo first order conditions, respectively), is commonly used to get insights into the binding mechanism and, in best scenarios, decipher whether conformationalselection, induced fit or even both mechanisms are at work. Therefore, we monitored the association kinetics of VirB9<sup>Ct</sup> with VirB7<sup>Nt</sup> under pseudo and reverse-pseudo first order conditions and at two different temperatures. At 25 °C and under pseudo first order conditions for VirB7Nt (varying [VirB7Nt] and keeping [VirB9<sup>Ct</sup>] constant), the experimental traces were found to be biexponential (Supporting Information, Figure S12A,B), indicating the occurrence of two events, as expected

for a coupled folding and binding process.  $^{7,22,53,54}$  The faster and the slower kinetic rate constants ( $k_{\rm obs}^1$  and  $k_{\rm obs}^2$ ) increased as a function of the ligand concentration (VirB7Nt), which is consistent with both the conformational selection (CS) and the induced-fit (IF) mechanisms (Figure 9A,B). The

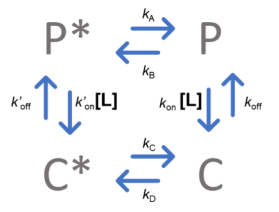


**Figure 8.** Cyclic model for a protein—ligand interaction mechanism. P and P\* denote conformational states of the protein, while C and C\* denote conformational states of the complex formed by the protein and its ligand.

ambiguity between these two mechanisms was resolved by performing the same kinetic experiment under reverse pseudo-first order conditions, i.e., varying the concentration of VirB9<sup>Ct</sup> while keeping [VirB7<sup>Nt</sup>] constant. The reverse pseudo-first order experiment yielded monoexponential kinetic traces (Supporting Information, Figure S12C,D), indicating that only a

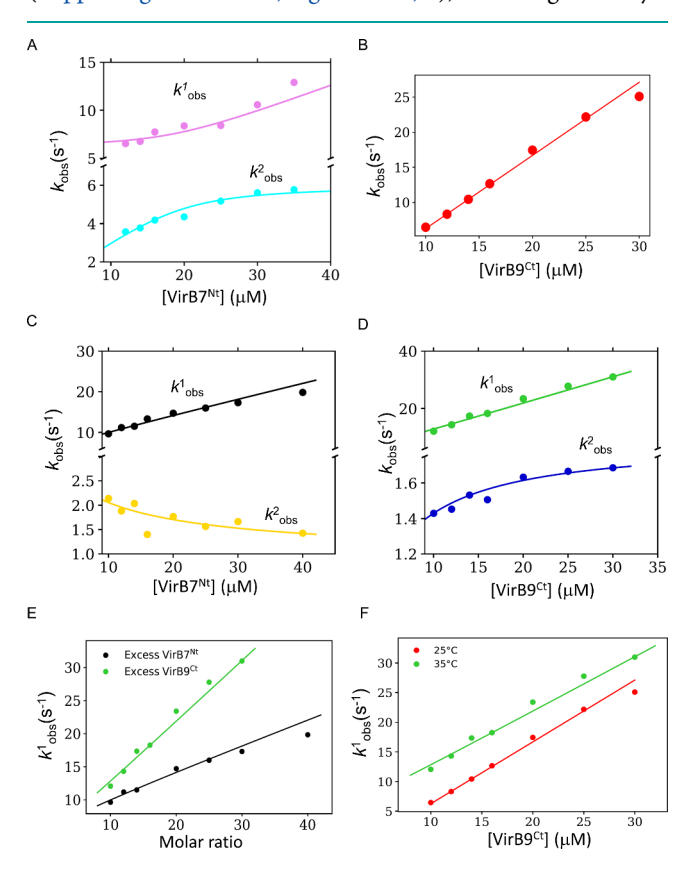


**Figure 9.** Observed kinetic rate constants from stopped flow fluorescence at 25 °C under excess of VirB7<sup>Nt</sup> (A) or under excess of VirB9<sup>Ct</sup> (B), fitted to the CS and to the lock and key model (one-step binding model), respectively. The observed kinetic rate constants obtained at 35 °C under an excess of VirB7<sup>Nt</sup> fitted to the CS model (C) or under an excess of VirB9<sup>Ct</sup> fitted to the IF model (D). Comparison between the faster kinetic rate constants ( $k_{\rm obs}^1$ ) at 35 °C under excess of VirB7<sup>Nt</sup> (black) or VirB9<sup>Ct</sup> (green) (E). Faster kinetic rate constants obtained under excess of VirB9<sup>Ct</sup> at 25 °C (red) and 35 °C (green) (F).

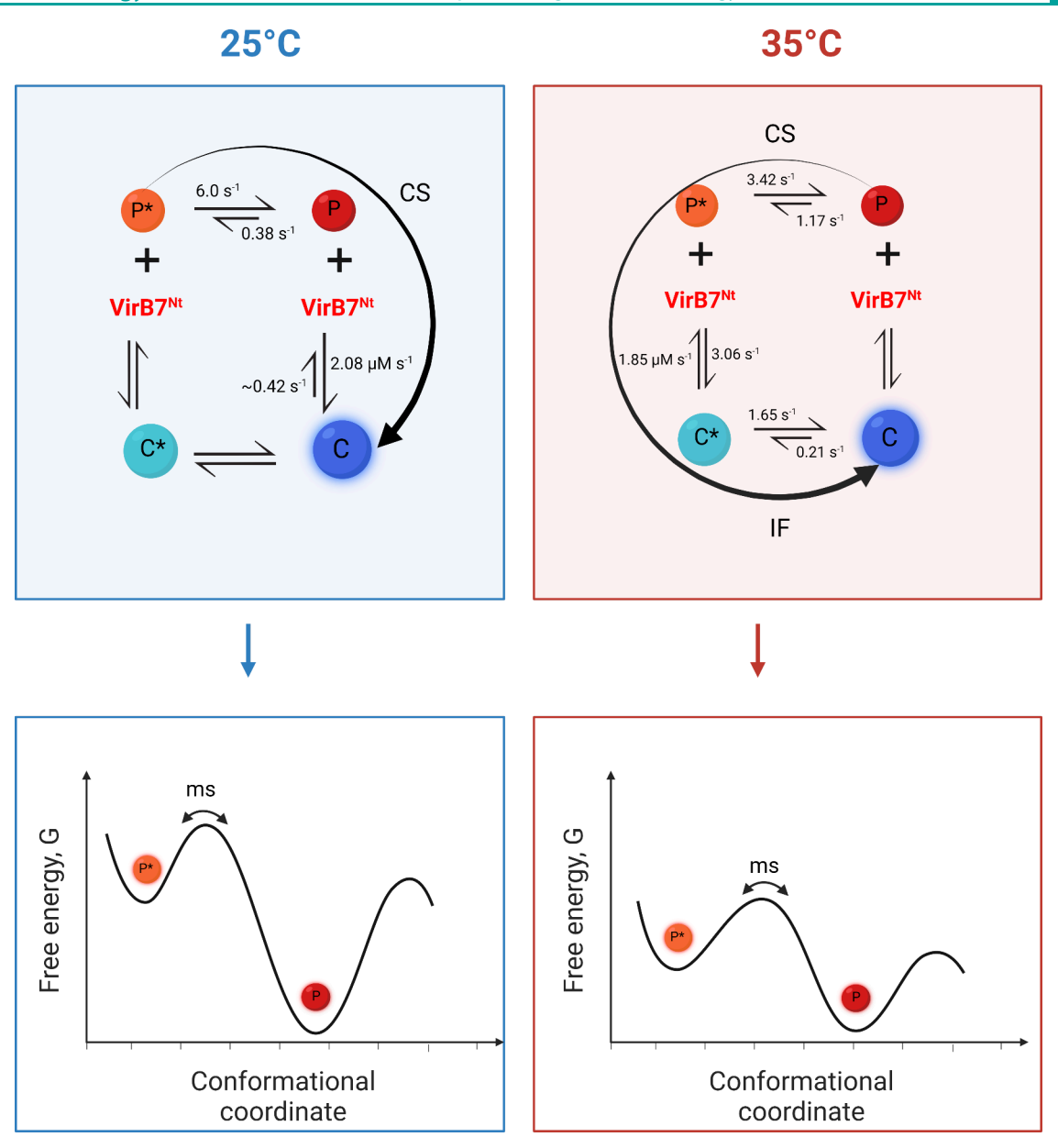


**Figure 10.** (Top) Possible VirB9<sup>Ct</sup>–VirB7<sup>Nt</sup> interaction pathways that were used to interpret the fluorescence stopped flow kinetic data obtained at 25 and 35 °C, with the kinetic rate constants of each step indicated on top of the corresponding arrow. (Bottom) Diagrams of the hypothetical conformational energy landscapes of the unbound VirB9<sup>Ct</sup> at 25 and 35 °C highlighting the relative free energies of the P and the P\* states (created with BioRender.com).

single step is being observed. This observed kinetic rate constant was shown to increase linearly with the VirB9 $^{\rm Ct}$  concentration, in agreement with a binding event (Figure 9C). These observations suggest that the VirB9 $^{\rm Ct}$  interaction with VirB7 $^{\rm Nt}$  could be described by a conformational-selection mechanism at 25 °C.  $^{53,55,56}$  When the kinetic experiments were repeated at 35 °C, the slower kinetic rate constant ( $k_{\rm obs}^2$ ) decreased hyperbolically as a function of [VirB7 $^{\rm Nt}$ ] (Figure 9D). This observed behavior of  $k_{\rm obs}^2$  is a kinetic signature of the conformational-selection mechanism.  $^{53,55}$ 

Interestingly, when the kinetic experiments at 35 °C were repeated under reverse pseudo-first order conditions, the experimental traces were biphasic (Supporting Information, Figure S13C,D) in contrast to what was observed at 25 °C (compare Figure 9C and E). Under these conditions, the fast and the slow kinetic rate constants,  $k_{\rm obs}^1$  and  $k_{\rm obs}^2$ , increased

linearly and hyperbolically with the VirB9<sup>Ct</sup> concentration, respectively (Figure 9D). The hyperbolic behavior of  $k_{\text{obs}}^2$ indicates that an additional event is observed at 35 °C. We hypothesized that this third event would be a conformational rearrangement of the complex after binding, i.e., an IF event that is observed only at the higher 35 °C temperature (Figure 9D). It is unclear why this third event was not observed under conditions of excess of VirB7Nt (Figure 9C). One possible explanation is that such IF event takes place at a time scale closer to  $k_{\text{obs}}^1$  resulting in a contaminated kinetic rate constant as suggested by its distorted behavior moving away from the linearity (Figure 9E-F). According to the experimental observations, we propose that the VirB9<sup>Ct</sup>–VirB7<sup>Nt</sup> association mechanism is best described as a four-state cyclic model (Figure 8). Here, P\* and P denote non-native and native-like conformations of VirB9<sup>Ct</sup>, respectively, in equilibrium with

Table 1. Values for the Fundamental Rate Constants Obtained from Fitting of the Stopped-Flow Kinetic Relaxations at 25 and 35 °C According to the CS and CS-IF Combined Model, Respectively

model	T (°C)	$k_{\rm A}~({ m s}^{-1})$	$k_{\mathrm{B}}~(\mathrm{s}^{-1})$	$k_{\rm on}~({ m s}^{-1}~\mu{ m M}^{-1})$	$k_{ m off}~({ m s}^{-1})$	$k_{\rm C}~({ m s}^{-1})$	$k_{\mathrm{D}}~(\mathrm{s}^{-1})$
CS-IF	35	≈3.42	≈1.17	≈1.85	≈3.06	≈1.65	≈0.21
CS	25	≈6.00	≈0.38	≈2.08	≈0.42		

one another. C\* and C denote an initial encounter complex and the final native complex, respectively.

In an attempt to better understand the kinetic behavior of our system, we fitted our data at 25 °C under conditions of excess of VirB7<sup>Nt</sup> to the CS model (eq 1 and Figure 10, left). This model assumes that, in the unbound state, VirB9<sup>Ct</sup> undergoes an equilibrium between two conformations, P and P\*, where P corresponds to the native (bound-like) VirB9<sup>Ct</sup> conformation selected to bind VirB7<sup>Nt</sup>. The fitted rate constants show that  $k_A \gg k_B$ , hence, according to the model, the population of P is much greater than P\* at this temperature (Figure 10, left). According to eq 6 (Supporting Information) the contribution of conformational changes to  $K_{\rm d}^{\rm app}$  is limited, as suggested by the fact that  $K_{\rm d}^{\rm int}$  ( $\approx$ 0.2  $\mu$ M) falls approximately in the same order of magnitude as the apparent  $K_{\rm d}^{\rm app}$  determined by ITC (Table 2).

Given the greater complexity of the association kinetics at 35  $^{\circ}$ C, we considered a three-step model (eq 2) for fitting the data (Figure 10, right). In this scenario, VirB7 $^{\text{Nt}}$  binds to VirB9 $^{\text{Ct}}$  in the P\* conformation, forming an initial encounter complex denoted C\* that will eventually rearrange to the final native complex conformation C. The kinetic constants  $k_{\rm C}$  and  $k_{\rm D}$  define the forward and reverse conformational exchange rate constants between the encounter complex and the final native-like complex, respectively (Figure 10, right). The three well-resolved phases observed at 35 °C were fitted to eq 2 (Figure 10, right, and Supporting Information, Figure S14). A comparison of the obtained approximate values for the kinetic rate constants (Table 1) shows that  $k_{\rm on}$  is nearly the same at 35 and 25 °C (Table 1), which is consistent with the nearly parallel behavior of  $k_{\rm obs}^1$  as a function of [VirB9<sup>Ct</sup>] at 25 and 35 °C (Figure 9F). In contrast,  $k_{\rm off}$  increased from  $\approx$ 0.42 s<sup>-1</sup> at 25 °C to 3.06 s<sup>-1</sup> at 35  $^{\circ}$ C, consistent with the greater  $K_{\rm d}^{\rm app}$  at 35  $^{\circ}$ C compared to 25  $^{\circ}$ C (Tables 1 and 2). The lower  $k_{\rm off}$  at 25 °C is consistent with the

Table 2. Experimental Values of  $K_{\rm d}^{\rm app}$  Obtained by ITC, and Calculated Values of  $K_{\rm d}^{\rm int}$  at 25 and 35 °C

temp (°C)	$K_{ m d}^{ m app} \; (\mu  m M)$	$K_{ m d}^{ m int} \ (\mu { m M})$
25	0.40	≈0.20
35	0.72	≈1.65

observed absence of chemical exchange between unbound and bound VirB9<sup>Ct</sup> when the CEST experiments were recorded at similar temperatures (Supporting Information, Figure S2). Notably, the calculated rate constants associated with the VirB9<sup>Ct</sup> conformational transitions ( $k_{\rm A}$  and  $k_{\rm B}$ ), highlight a change in the equilibrium between native (P) (bound-like) and non-native (P\*) VirB9<sup>Ct</sup> conformations as a function of temperature. This conclusion is supported by the temperature-dependence of the equilibrium constant between P\* and P, given by  $k_{\rm A}/k_{\rm B}$ , which changed from 15.8 at 25 °C to 2.92 at 35 °C (Table 1 and Figure 10, bottom). This VirB9<sup>Ct</sup> conformational ensemble redistribution at 35 °C is in agreement with the large temperature dependence of the VirB9<sup>Ct</sup> NMR spectrum (Figure 4 and Supporting Information, Figures S1 and S7).

In summary, kinetic data obtained at 25 and 35 °C suggest that conformational selection is the main binding mechanism between VirB7<sup>Nt</sup> and VirB9<sup>Ct</sup>. However, at 35 °C, the greater populations of distinct VirB9<sup>Ct</sup> conformations could increase the probability of additional binding pathways, in which the formation of initial non-native encounter complexes is followed by conformational rearrangements toward the native complex (Figure 10, top). These two binding pathways (Figure 8) might compete with each other for the formation of the final complex. The predominance of one or the other binding pathway seems to be determined by the temperature-dependent balance of the VirB9<sup>Ct</sup> conformational equilibrium (Figure 10, bottom).

Computer Simulation of the Free Energy Landscape of the VirB9Ct-VirB7Nt Coupled Folding and Binding **Process.** Simulations of the structure-based model (SBM)<sup>57</sup> in an all-atom representation of the VirB9<sup>Ct</sup>-VirB7<sup>Nt</sup> complex were executed in a wide range of temperatures that sampled binding and folding of the protein and peptide chains. The configurational search was enhanced with simulations at temperatures close to the VirB9<sup>Ct</sup>–VirB7<sup>Nt</sup> binding temperature  $(T_{\rm bind})$ , where binding/unbinding events had roughly equal probabilities to occur. The many long-run simulations sampled the complex configurational space and were analyzed by the thermodynamic WHAM algorithm.<sup>58</sup> Figure 11 shows the resulting thermodynamic Helmholtz free energy surface (F) of the VirB9<sup>Ct</sup>-VirB7<sup>Nt</sup> recognition process. F is displayed along two reaction coordinates that count the number of native contacts: the intramolecular folding of VirB9<sup>Ct</sup>  $(Q_{\text{fold}})$  and the intermolecular binding contacts between VirB9<sup>Ct</sup> and VirB7<sup>Nt</sup>  $(Q_{\rm bind})$ . At  $T_{\rm bind}$ , the simulated system displayed three stable free energy minima and one metastable state (Figure 11). Two of them correspond to the unbound VirB9<sup>Ct</sup> state, and were indicated as P and P\* in analogy with the intermediate states highlighted by the stopped flow fluorescence data. Following the same analogy, the metastable and the stable bound-state free energy basins were depicted C\* and C, respectively (Figure 11). Figure 11B shows an illustrative time trajectory of the complex projected over F with representative structures of the three F minima (P\*, P, and C) and of the metastable C\* state. The time trajectory window is also plotted in Figure 11C. It is noteworthy that complex dissociation leads to a minimum free energy basin along which VirB9<sup>Ct</sup> is partially folded, indicated by P\* in Figure 11C.

This theoretical experiment showed that starting from the unbound and partially folded  $P^*F$  basin in Figure 11B, there is a small energetic F barrier ( $\sim 1k_BT$ ) along the VirB9<sup>Ct</sup> folding coordinate to the still unbound but folded P ensemble (between P and  $P^*$ ) (Figure 11B). From there, VirB9<sup>Ct</sup> is able to bind to VirB7<sup>Nt</sup> after crossing F barriers of about  $9k_BT$  via the  $C^*$  metastable state or directly to the folded and bound C native state of VirB9<sup>Ct</sup>–VirB7<sup>Nt</sup>. It is also possible to concomitantly fold and bind from the  $P^*$  to the  $C^*$  and then C or directly to C, although the probability is lower (free energy barriers are higher). These are the proposed folding and binding mechanisms of VirB9<sup>Ct</sup> and VirB7<sup>Nt</sup> discussed in the previous sections. It is a direct consequence of the energy landscape

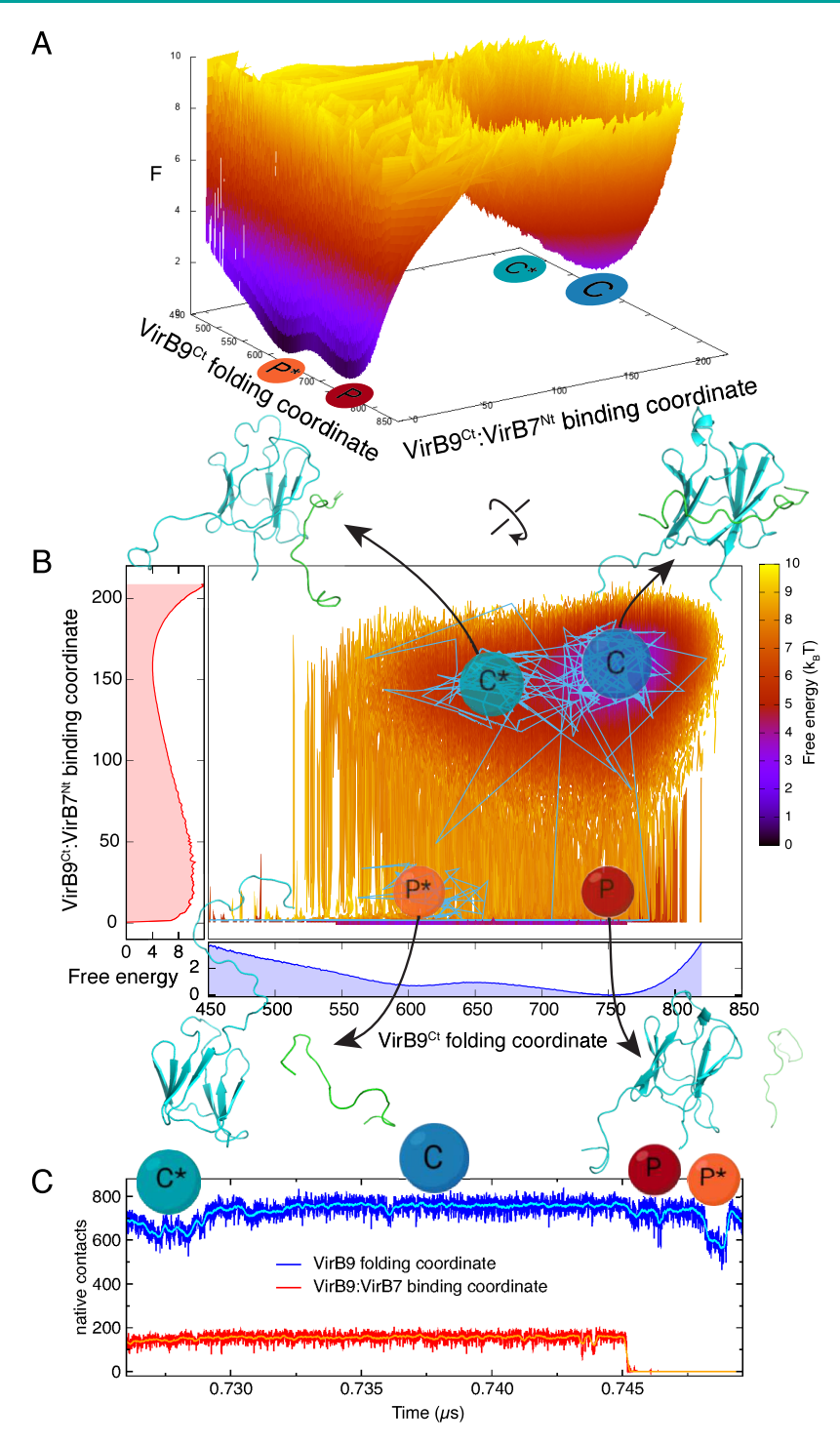


**Figure 11.** Simulation of the VirB9<sup>Ct</sup>–VirB7<sup>Nt</sup> folding and binding free energy landscape using molecular dynamics. (A) Two-dimensional free energy (F) profile as a function of the number of VirB9<sup>Ct</sup> intramolecular native contacts ( $Q_{\rm fold}$ ) and VirB7<sup>Nt</sup>–VirB9<sup>Ct</sup> intermolecular contacts ( $Q_{\rm bind}$ ). (B) F in map view of (A) and the one-dimensional F projections as a function of  $Q_{\rm bind}$  (in red) and of  $Q_{\rm fold}$  (in blue). In (B), it is also shown an illustrative time trajectory of the protein complex projected over the F landscape with representative structures of the three F minima ( $P^*$ , P, and C) and of the metastable  $C^*$  state. (C) Time trajectories of the reaction coordinates  $Q_{\rm bind}$  (in red) and  $Q_{\rm fold}$  (in blue) for the complex and their respective averages over each 50 frames in cyan and orange as guide to the eyes. (A)–(C) are presented at the binding temperature ( $T_{\rm bind}$ ) and F profiles are in units of the thermal  $K_{\rm B}$  with  $K_{\rm B}$  being the Boltzmann constant (created with BioRender.com).

theory that accommodates the conformational selection and the induced fit mechanisms over a funneled surface toward the lowest energy basin containing the folded-bound conformation.  $^{59-61}$ 

# CONCLUSIONS

We showed previously that VirB7<sup>Nt</sup> behaves as a random coil and that VirB9<sup>Ct</sup> is intrinsically dynamic in the unbound state.<sup>29</sup> In this work, we combined different biophysical techniques with computer simulations to characterize the VirB9<sup>Ct</sup>–VirB7<sup>Nt</sup>

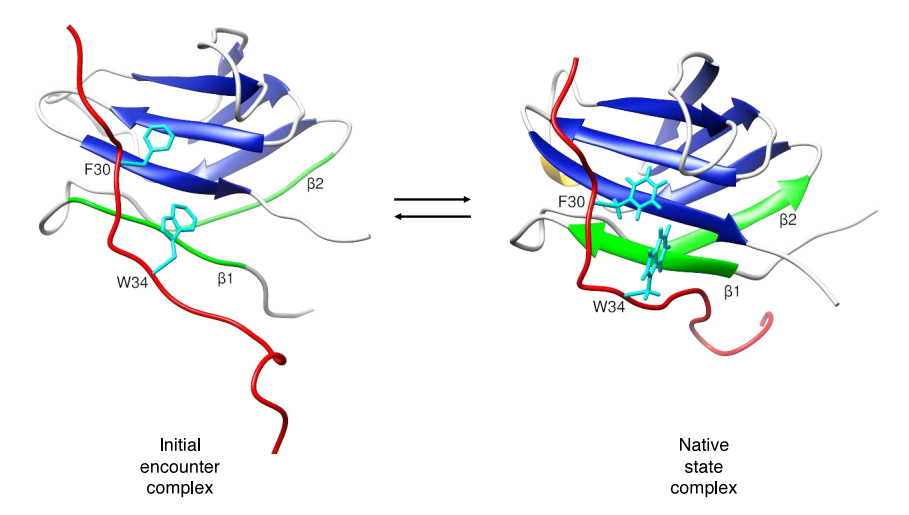


**Figure 12.** Snapshots of VirB7<sup>Nt</sup>–VirB9<sup>Ct</sup> initial encounter (left) and native state (right) complexes, corresponding to the complex metastable state (C\*) and the bound state (C) conformational energy basin of Figure 11. VirB9<sup>Ct</sup>  $\beta$ -strands  $\beta$ 1 and  $\beta$ 2 are colored green, while VirB7<sup>Nt</sup> is shown in red. This orientation shows VirB7<sup>Nt</sup> W34 and F30 positioned to make contact with residues on the surface of the VirB9<sup>Ct</sup>  $\beta$ 1– $\beta$ 8– $\beta$ 7– $\beta$ 4  $\beta$ -sheet.

coupled folding and binding mechanism. NMR data obtained for VirB9<sup>Ct</sup> in the unbound state at 35 °C showed strong evidence that  $\beta$ 1 is unstructured in the absence of VirB7<sup>Nt</sup>, while other residues also located at the VirB7Nt binding region experience an equilibrium between multiple conformations at the millisecond time scale. At 25 °C VirB9<sup>Ct</sup> seems to be partially confined in a bound-like conformational space basin, which favors conformational selection as the dominant binding mode. In contrast, at 35 °C the energy barriers between different VirB9<sup>Ct</sup> conformations are more easily surpassed, giving rise to different VirB9<sup>Ct</sup> conformations and, hence, to other binding pathways involving the formation of initial encounter complexes that will eventually rearrange to the final native conformation. Indeed, analysis of the C\* complex metastable state snapshots during the molecular dynamics simulations at  $T_{\text{bind}}$  showed that  $\text{VirB7}^{\text{Nt}}$  may first anchor itself to  $\text{VirB9}^{\text{Ct}}$  by making intermolecular contacts at the surface of the  $\beta 1 - \beta 8 - \beta 7 - \beta 4$  $\beta$ -sheet prior to  $\beta$ 0 formation (Figure 12). The present scenario calls attention to the fact that, similarly to the folding process, coupled folding and binding involves searching for the most favored intramolecular and intermolecular interactions on a rugged and funnelled conformational energy landscape, in which multiple intermediates may lead to the final native state.

$$P^* \stackrel{k_A}{\rightleftharpoons} P \stackrel{k_{on}[L]}{\rightleftharpoons} C \tag{1}$$

$$P \stackrel{k_{B}}{\rightleftharpoons} P^{*} \stackrel{k_{on}[L]}{\rightleftharpoons} C^{*} \stackrel{k_{C}}{\rightleftharpoons} C \tag{2}$$

#### EXPERIMENTAL SECTION

**Expression and Purification of VirB9**<sup>Ct</sup>. BL21(DE3) *Escherichia coli* cells harboring the plasmid pET28a containing the gene encoding VirB9<sup>Ct</sup> (residues 154–255) were grown in either M9 or LB medium supplemented with 50  $\mu$ g/mL of kanamycin at 37 °C. <sup>29</sup> Isotopically enriched protein samples were expressed in M9 in the presence of 2 g/L and/or 0.5 g/L of <sup>13</sup>C uniformly labeled glucose and <sup>15</sup>N ammonium chloride, respectively. Protein expression was induced by the addition of 0.5 mM of isopropyl-1-thio- $\beta$ -D-galactopyranoside (IPTG) when the optical density at 600 nm (OD<sub>600</sub>) reached 0.8 and carried out overnight at 18 °C. Cells were harvested by centrifugation for 1 h at

5000 rpm and 4 °C on a Beckman centrifuge using rotor JLA-10. The cell pellet was suspended in lysis buffer (20 mM Tris/HCL pH 7.5, 1 mM PMSF, 0.5 mg mL<sup>-1</sup> lysozyme) and stored at -20 °C until further use. Cell lysis was carried out by sonication. The lysate was clarified by centrifugation for 1 h at 13000 rpm on a Beckman centrifuge equipped with rotor JA-20. The supernatant was loaded on a Hiprep FF 16/10 SP Sepharose column (GE Healthcare), pre-equilibrated with buffer A (20 mM Tris/HCL pH 7.5). VirB9<sup>Ct</sup> eluted during a linear NaCl gradient with buffer B (20 mM Tris/HCl pH 7.5 and 700 mM NaCl) over 14 column volumes (CV). Eluted fractions were pooled and loaded onto a Ni<sup>2+</sup>-HiTrap column (GE Healthcare), pre-equilibrated with buffer A (20 mM Tris/HCl pH 7.5, 200 mM NaCl, and 20 mM imidazole). VirB9<sup>Ct</sup> eluted during a linear concentration gradient of imidazole with buffer B (20 mM Tris/HCl pH 7.5, 200 mM NaCl, and 500 mM imidazole). The imidazole was removed by buffer exchange to 20 mM Tris/HCl pH 7.5, and VirB9<sup>Ct</sup> was concentrated to a final volume of 1 mL using an Amicon Ultra Device with a cutoff of 3 kDa. Cleavage of the histidines tag was carried out by a 3 h incubation with 100–200  $\mu$ L of thrombin-agarose resin (Sigma-Aldrich) in 50 mM Tris-HCl pH 8.0 containing 10 mM CaCl<sub>2</sub>. Subsequently, this sample was loaded onto the Ni<sup>2+</sup>-HiTrap column equilibrated with buffer A and cut VirB9<sup>Ct</sup> was found in the flowthrough. The isolated protein buffer was exchanged to 20 mM sodium acetate pH 5.5 containing 50 mM NaCl. Concentrated protein samples were stored at 4 °C or frozen at −20 °C until further use. Protein concentration was calculated from the absorbance at 280 nm using the molar extinction coefficient  $\epsilon = 17420 \text{ M}^{-1} \text{ cm}^{-1}$ .

**Preparation of the VirB7**<sup>Nt</sup> **Peptide.** A synthetic peptide with the amino acid sequence TKPAPDFGGR WKHVNHFDEAPTE, corresponding to VirB7 residues 24 to 46 (VirB7<sup>Nt</sup>), was purchased from Biomatik. The peptide was acetylated at the N-terminal end and amidated at the C-terminal end. VirB7<sup>Nt</sup> samples were prepared by dissolving the required peptide mass in 20 mM sodium acetate pH 5.5 with 50 mM NaCl, or in 20 mM sodium phosphate pH 7.5 with 10 mM NaCl. Peptide concentration was calculated by the absorbance at 280 nm assuming  $\epsilon = 5500 \, \mathrm{M}^{-1} \, \mathrm{cm}^{-1}$ .

**NMR Experiments.** All NMR measurements were performed on a Bruker AVANCE III spectrometer operating at 800 MHz ( $^{1}$ H field) and equipped with a TCI cryoprobe. All NMR spectra were processed with NMRPipe and analyzed using the CcpNmr Analysis software version 2.4. $^{62,63}$  NMR samples contained approximately 500  $\mu$ M of protein dissolved in 20 mM sodium acetate pH 5.5, containing 50 mM of NaCl and 10% of D<sub>2</sub>O. Substoichiometric VirB9<sup>Ct</sup>–VirB7<sup>Nt</sup> samples used for the CEST experiments were prepared by adding the appropriate amount of unlabeled VirB7<sup>Nt</sup> dissolved in the same buffer as VirB9<sup>Ct</sup>. CEST experiments were recorded in pseudo-3D fashion by

incrementing the weak <sup>15</sup>N saturation field carrier frequency during the exchange period,  $T_{\rm ext}$  of 400 ms. A reference spectrum was recorded skipping the exchange period. CEST  $I/I_0$  profiles were extracted and visualized using in-house scripts made for MATLAB R2015a or Python. The  $^{15}$ N-CEST  $I/I_0$  profiles recorded with weak saturation frequencies  $\gamma_{\rm N} B_1/2\pi = 15$  and 30 Hz were simultaneously fitted to the Bloch-McConnell equation assuming a two-states exchange model using an in-house Python script that uses a Bayesian approach as described.<sup>64</sup> Uncertainties in the cross peak intensities were taken from the noise level in each spectrum. The  $\gamma_{\rm N}B_1/2\pi$  saturation field and the experimental bound state  $^{15}N$  chemical shifts  $(\Omega_{\rm B})$  were constrained with Gaussian priors of  $\sigma$  = 1% and 5%, respectively. Unless otherwise stated, all CEST figures were prepared with experiments recorded using saturation frequency  $\gamma_N B_1/2\pi = 15$  Hz. VirB9<sup>Ct</sup> random coil <sup>15</sup>N chemical shifts were predicted using the online predictor server ncIDP.<sup>51</sup> Backbone ( ${}^{1}HN$ ,  ${}^{15}N$ ,  ${}^{13}C\alpha$ ,  ${}^{13}CO$ ) and side chain ( ${}^{13}C\beta$ ) resonance assignments for VirB9<sup>Ct</sup> in the unbound state were obtained through the analysis of a set of triple resonance NMR experiments recorded at 7 °C and deposited in the BMRB under the accession code 51836. Assignments for the unbound VirB9<sup>Ct 1</sup>H-<sup>15</sup>N cross peaks at 35 °C (Figure S6) were transferred from those obtained at 7 °C using a series of HSQC experiments recorded at increasing temperatures from 7 up to 35 °C in steps of 3 °C. Additional assignments were obtained from the analysis of a longitudinal exchange HSQC experiment,<sup>65</sup> recorded with a mixing time of 400 ms on a sample of <sup>15</sup>N labeled VirB9<sup>Ct</sup> and unlabeled VirB7<sup>Nt</sup> at the 1:06 (VirB9<sup>Ct</sup>:VirB7<sup>Nt</sup>) molar ratio. Using this approach 83 <sup>1</sup>H-<sup>15</sup>N spin pairs were assigned at 35 °C and deposited in the BMRB under the accession code 52005. Backbone resonance assignments for VirB9<sup>Ct</sup> and VirB7<sup>Nt</sup> in the bound state (35  $^{\circ}$ C) were obtained from the BMRB entry 25512. $^{29}$ 

**Circular Dichroism.** Circular dichroism (CD) spectra were recorded on a Jasco J720 (Jasco, Japan) spectropolarimeter at 25 °C, from 190 to 260 nm using integration step of 1 nm, scanning speed of 50 nm/min and accumulation of 6 scans. Samples were prepared at  $10~\mu\mathrm{M}$  protein concentration in 20 mM sodium phosphate pH 7.26 with 10 mM NaCl, and transferred to 1 mm path-length quartz cells. A spectrum of the buffer was recorded with the same acquisition parameters as the protein sample and subtracted as blank. Deconvolution of the VirB9<sup>Ct</sup> CD spectrum was carried out with the online server DICHROWEB using the CDSSTR method and data set #7 that includes globular and denatured protein spectra.  $^{35,66-68}$ 

Denaturation experiments were performed on a Jasco J-815 spectropolarimeter using a 1 mm path-length cell. Far UV-CD spectra were recorded from 190 to 260 nm, using integration step of 1 nm, scanning speed of 100 nm/min and accumulation of 3 scans. The temperature was increased from 25 to 95  $^{\circ}\mathrm{C}$  in steps of 5  $^{\circ}\mathrm{C}$ . The behavior of the elipticity at at 215 and 233 nm as a function of temperature was fitted to the following equation assuming a two-state equilibrium:

$$\Theta_{\lambda}(T) = S_{N} \left( \frac{1}{1 + \exp \frac{-\Delta H}{RT} \left( 1 - \frac{T}{T_{m}} \right)} \right) + S_{D} \left( \frac{1}{1 + \exp \frac{\Delta H}{RT} \left( 1 - \frac{T}{T_{m}} \right)} \right)$$
(3)

where  $\theta$ ,  $S_{\rm N}$ , and  $S_{\rm D}$  refer to the observed, native state and denatured state elipticities, respectively, at a given wavelength. The terms within brackets refer to the populations of native and denatured states.  $\Delta H$  and  $T_{\rm m}$  refer to the denaturation enthalphy and the melting temperature, respectively. Fitting to eq 3 assumed  $\Delta H$ ,  $T_{\rm m}$ ,  $S_{\rm N}$ , and  $S_{\rm D}$  as free parameters. The sloping baselines before and after the denaturation transition were modeled replacing the  $S_{\rm N}$  and/or  $S_{\rm D}$  signal with a straight line equation as a function of temperature:

$$S_{LN/D}(T) = mT + b \tag{4}$$

where T is the temperature, m is the slope, and b is the intercept with the y axis.<sup>69–71</sup>

**ANS Fluorescence.** The fluorescence spectra of 1-anilino-8-naphthalenesulfonic acid (ANS) were recorded with a Hitachi F-7000 FL spectrofluorometer using excitation wavelength ( $\lambda_{ex}$ ) of 375

nm. The emission wavelength ( $\lambda_{\rm em}$ ) was scanned from 400 to 650 nm at 25 °C. A 2 mM ANS stock solution was prepared in 20 mM sodium acetate buffer (pH 5.5) containing 50 mM NaCl. Stock protein and peptide solutions were prepared in the same buffer. The ANS concentration was estimated using  $\epsilon_{350}=4950~{\rm M}^{-1}~{\rm cm}^{-1.72}$  All fluorescence samples consisted of 10  $\mu$ M of protein and/or peptide plus 250  $\mu$ M of ANS in the same buffer. Samples were preincubated for 30 min before fluorescence measurements.

**Isothermal Titration Calorimetry.** Isothermal titration calorimetry experiments were performed on a VP-ITC micro calorimeter (MicroCal incorporated). Protein and peptide samples were prepared in the same buffer that consisted in 20 mM sodium acetate pH 5.5 and 50 mM NaCl. All measurements were performed in triplicate, at temperatures of 10, 25, and 35  $^{\circ}$ C. Titrations were carried out with 20  $\mu$ M of VirB7<sup>Nt</sup> peptide in the calorimeter cell and 200  $\mu$ M of VirB9<sup>Ct</sup> in the syringe using 20–25 injections of 5  $\mu$ L. Control experiments were carried out by titrating buffer in the peptide. Data analysis was carried out using OriginLab7.0 and the standard supplier software for  $K_d$  (here called  $K_d^{app}$ , which considers the effects of conformational changes to the intrinsic value of  $K_d$ ) and  $\Delta H$  estimation. Additionally, a set titrations of the peptide at 10, 15, and 20  $\mu$ M with VirB9<sup>Ct</sup> at 150  $\mu$ M were carried out at 35 °C. The resulting isotherms crossed each other at the same inflection point; they were simultaneously fitted to the one-site binding stoichiometric model to determine the  $K_{\rm d}^{\rm app}$  at 35 °C as described previously. 64 Briefly, the stoichiometry of the complex was constrained at n = 1 with a narrow Gaussian prior with  $\sigma = 0.01$ , while the peptide concentrations were allowed to vary as free parameters.

**Differential Scanning Calorimetry.** Differential scanning calorimetry experiments were performed on a VP-DSC microcalorimeter (MicroCal incorporated) with a scan rate of 60 °C/h. All samples were prepared in 20 mM sodium acetate pH 5.5 containing 50 mM of NaCl. The concentrations of the unbound VirB9<sup>Ct</sup> and of the VirB9<sup>Ct</sup>–VirB7<sup>Nt</sup> 1:1 complex were 300  $\mu$ M. All measurements were performed in triplicate and were reproducible.

**Stopped Flow Kinetics.** Kinetic experiments were carried out using an Applied Photophysics stopped-flow spectrofluorometer. The reaction course was followed by measuring the VirB7<sup>Nt</sup> and VirB9<sup>Ct</sup> Trp fluorescence intensities at  $\lambda_{em}=350$  nm, with  $\lambda_{ex}=280$  nm. Samples were prepared in 20 mM sodium acetate pH 5.5, containing 50 mM of NaCl. All experiments were performed under pseudo-first order conditions at 1  $\mu$ M concentrations of VirB9<sup>Ct</sup> or VirB7<sup>Nt</sup> with increasing VirB9<sup>Ct</sup> or VirB7<sup>Nt</sup> concentrations (from 10 up to 40  $\mu$ M), respectively. Each kinetic trace was fitted to either single or double exponential functions using the proData software (Applied photophysics) to extract the observed rate constant(s) ( $k_{obs}$ ) at each concentration. Each  $k_{obs}$  corresponded to the average  $k_{obs}$  value from 3 to 5 fitted traces.

The kinetic data at 25 °C recorded under excess of [VirB7Nt] was fitted to eq 3 from the Supporting Information, corresponding to the general CS case. 53,55 The conformational exchange rate constants from (eq 1)  $k_A$  and  $k_B$ , as well as the association constants  $k_{on}$  and  $k_{off}$ , were considered as free parameters. The experimental data at 35 °C were fitted to the combined CS-IF model (eq 2). According to the CS-IF combined model from eq 2, the binding event is shared between the independently CS and IF steps. Briefly,  $k_{\text{obs}}^2$  values obtained under excess of  $VirB7^{Nt}$  were adjusted with the CS part of the model assuming the rapid equilibrium approximation according to eq 5 in the Supporting Information. The values of  $k_{\rm obs}^1$  and  $k_{\rm obs}^2$  obtained under excess of VirB9<sup>Ct</sup> were adjusted with eq 4 from the Supporting Information, corresponding to the IF part of the model. To further restrict the parameters' space we used the  $K_{\rm d}^{\rm app}$  obtained by ITC at 35 °C as an additional experimental information.  $K_d^{app}$  refers to the equilibrium dissociation constant that considers the contribution of conformational exchange to the intrinsic value of  $K_d$  (here called  $K_d^{int}$ ). It is worthy noting that  $K_{\rm d}^{\rm app,CS-IF}$  and  $K_{\rm d}^{\rm int}$  in the combined CS-IF model, depend on each other according to eq 7 in the Supporting Information.

Overall, the fitting was implemented in a Python routine using a Bayesian approach, considering  $k_{\rm on}$ ,  $k_{\rm off}$ ,  $k_{\rm A}$ ,  $k_{\rm B}$ ,  $k_{\rm C}$ , and  $k_{\rm D}$  as free parameters, while  $k_{\rm obs}^2$  obtained under excess of VirB7<sup>Nt</sup> and  $k_{\rm obs}^1$  and  $k_{\rm obs}^2$  obtained under excess of VirB9<sup>Ct</sup>, as well as the  $K_{\rm d}^{\rm app}$  obtained from ITC

at 35 °C, were given as input. The latter was constrained by a Gaussian prior with a value centered at  $K_{\rm d}^{\rm app}=0.723~\mu{\rm M}$  and a confidence interval of 0.082  $\mu{\rm M}$ . MCMC sampling was carried out with 200 chains of 3000 points each, and a burning of 2000 points. Flat priors were introduced to restraint the range of the free parameters:  $0.001 \le k_{\rm A} \le 10.0$ ,  $0.001 \le k_{\rm B} \le 10.0$ ,  $0.001 \le k_{\rm O} \le 10.0$ ,  $0.001 \le k_{\rm C} \le 10.0$ , and  $0.00001 \le k_{\rm D} \le 2.0$  in units of s<sup>-1</sup>. Fitted parameters probability distributions and their correlations are shown in the Supporting Information, Figure S14.

Molecular Dynamic Simulations. MD Simulations of Unbound and Bound VirB9<sup>Ct</sup>. Molecular dynamic (MD) simulations of unbound and bound VirB9<sup>Ct</sup> were computed using Amber FF99SBnmr2 forcefield.<sup>73</sup> The first model of the VirB9<sup>Ct</sup>–VirB7<sup>Nt</sup> NMR ensemble (PDB 2N01) was used as starting structure. For the unbound VirB9<sup>Ct</sup> computer simulation, we removed the peptide from the model using the UCFS chimera tool. The system conditions were prepared using GROMACS v2018.6.<sup>74</sup> All systems were then explicitly solvated with TIP4P water models in a cubic box (10.5 × 7.0 × 7.0 nm) and neutralized keeping NaCl concentration at 50 mM (15 Na<sup>+</sup> and 23 Cl<sup>-</sup>ions). Protein charges at pH 5.0 were determined using Propka version 3.0.<sup>75</sup> The systems were equilibrated consecutively in isothermal—isochoric (NVT) and isothermal—isobaric (1 bar; NpT) ensembles at 308 K for 2000 ps. The unbound and bound VirB9<sup>Ct</sup> MD simulations were run for 4000 and 1000 ns, respectively.

MD Simulation of the Interaction Mechanism. The structurebased model (SBM),<sup>76</sup> formerly known as Go-model<sup>77</sup> has its foundation on the energy landscape theory.<sup>59</sup> SBM was used to simulate the VirB9<sup>Ct</sup>–VirB7<sup>Nt</sup> complex with all-heavy (non-hydrogen) atoms. SBMs is a topology-based model that defines the energy minimum of the Hamiltonian function as the native conformation, i.e., the model has minimal intrinsic energetic frustration.  $^{80,81}$  The simulation protocol was based in the previous works.  $^{61,82}$  SMOG2 version 2.3-beta with standard options for the all-atom model prepared the input files for the SBM simulations. 83 Simulations were executed with the GROMACS suite 5.1.4.<sup>74</sup> The thermodynamic analysis was performed over 50 temperature runs from lower temperatures (fully folded and bound states) to higher temperatures (unbound states), including the transition temperature between the on and off states (  $T_{\rm bind}$  ). Each simulation was executed over 1  $\mu$ s with integration steps of 2 fs and snapshots were recorded every 4 ps. The results are shown in reduced units of GROMACS for temperature and energy, commonly used in coarse-grained SBMs.  $^{76}$  Thus, energy is in units of  $k_{\rm B}T$ , and the time unit is not as the real one. Thermodynamic calculations were executed by the Weighted Histogram Analysis Method (WHAM)<sup>58,84</sup> implemented in the PyWham package and BASH scripts.<sup>85</sup> WHAM computes the microcanonical density of states that is used to build the free energy profiles.  $T_{\rm bind}$  was defined as the peak found in the theoretical specific heat curve in temperature  $(C_{\nu}(T))$ . The number/ fraction of native contacts within a given structure (Q) was used to evaluate the nativeness along the reaction coordinate, which describes how similar is a given structure with respect to the reference native structure. Root mean square fluctuation (rmsf), radius of gyration  $(R_{\circ})$ , root-mean-square deviation (rmsd) and distance between two chains (d) were computed with the analysis package contained in the GROMACS suite. Protein structures were visualized with PyMOL (https://pymol.org), VMD, 86 and UCSF Chimera 87 softwares. Twoand three-dimensional curves were plotted with Grace (https:// plasma-gate.weizmann.ac.il/Grace), Gnuplot (http://www.gnuplot. info), and Matplotlib<sup>88</sup> packages. The analysis codes were implemented in Python (https://python.org) using Jupyter Notebooks with native libraries, such as NumPy, SciPy, and Pandas.

#### ASSOCIATED CONTENT

# Supporting Information

The Supporting Information is available free of charge at https://pubs.acs.org/doi/10.1021/acschembio.3c00649.

Section 1: Kinetic background theory equations used to fit stopped-flow fluorescence data to kinetic models. Section 2: Supplementary figures <sup>15</sup>N HSQC spectra, <sup>15</sup>N CEST

data, analysis of molecular dynamics trajectories, and kinetics data of  $VirB9^{Ct}$  alone and in the presence of  $VirB7^{Nt}$  (PDF)

#### AUTHOR INFORMATION

#### **Corresponding Author**

Roberto Kopke Salinas — Department of Biochemistry, Institute of Chemistry, University of São Paulo, São Paulo 05508-000, Brazil; orcid.org/0000-0003-1032-7683; Email: roberto@iq.usp.br

#### **Authors**

Angy Liseth Dávalos – Department of Biochemistry, Institute of Chemistry, University of São Paulo, São Paulo 05508-000,
Brazil

José David Rivera Echeverri — Department of Biochemistry, Institute of Chemistry, University of São Paulo, São Paulo 05508-000, Brazil; oorcid.org/0000-0002-4172-7869

Denize C. Favaro — Department of Organic Chemistry, State University of Campinas, Campinas 13083-862, Brazil; Structural Biology Initiative, CUNY Advanced Science Research Center, New York, New York 10031, United States; orcid.org/0000-0001-5563-2548

Ronaldo Junio de Oliveira — Department of Physics, Institute of Exact, Natural and Educational Sciences, Federal University of Triângulo Mineiro, Uberaba 38064-200, Brazil;
ocid.org/0000-0003-4860-309X

Gustavo Penteado Battesini Carretero – Department of Biochemistry, Institute of Chemistry, University of São Paulo, São Paulo 05508-000, Brazil

Caroline Lacerda — Department of Biochemistry, Institute of Chemistry, University of São Paulo, São Paulo 05508-000, Brazil

Iolanda Midea Cuccovia — Department of Biochemistry, Institute of Chemistry, University of São Paulo, São Paulo 05508-000, Brazil

Marcus Vinicius Cangussu Cardoso — Department of Biochemistry, Institute of Chemistry, University of São Paulo, São Paulo 05508-000, Brazil; Present Address: Department of Chemistry, Institute of Exact and Biological Sciences, Federal University of Ouro Preto, Ouro Preto, 35400-000, Brazil; ⊚ orcid.org/0000-0001-5124-0432

Chuck S. Farah – Department of Biochemistry, Institute of Chemistry, University of São Paulo, São Paulo 05508-000, Brazil

Complete contact information is available at: https://pubs.acs.org/10.1021/acschembio.3c00649

#### Notes

The authors declare no competing financial interest.

### ACKNOWLEDGMENTS

The authors thank the Analytical Instrumentation Center of the University of São Paulo for providing access to the 800 MHz NMR instrument. This work was supported by grants from the São Paulo Research Foundation (FAPESP 2017/17303-7), the Minas Gerais Research Foundation (FAPEMIG APQ-02303-21), and the Conselho Nacional de Desenvolvimento Científico e Tecnológico (CNPq 312328/2019-2). Computational resources were provided by the "Núcleo de Computação Científica da Universidade do Estado de São Paulo" (NCC/GridUnesp) and the "Centro Nacional de Processamento de

Alto Desempenho" in São Paulo (CENAPAD-SP). A.L.D. received a CNPq Ph.D. Fellowship (141398/2018-3). R.K.S. receives a CNPq Research Fellowship (308119/2020-7). J.D.R. and M.V.C.C. received FAPESP Postdoctoral Fellowships (2018/21450-8 and 2016/17375-5).

## REFERENCES

- (1) Dunker, A.; et al. Intrinsically disordered protein. *Journal of Molecular Graphics and Modelling* **2001**, 19, 26–59.
- (2) Uversky, V. N.; Dunker, A. K. Understanding protein non-folding. *Biochimica et Biophysica Acta Proteins and Proteomics* **2010**, 1804, 1231–1264.
- (3) Tompa, P. Intrinsically unstructured proteins. *Trends Biochem. Sci.* **2002**, 27, 527–533.
- (4) Dyson, H. J.; Wright, P. E. Intrinsically unstructured proteins and their functions. *Nat. Rev. Mol. Cell Biol.* **2005**, *6*, 197–208.
- (5) Van Der Lee, R.; et al. Classification of intrinsically disordered regions and proteins. *Chem. Rev.* **2014**, *114*, 6589–6631.
- (6) Fuxreiter, M. Fuzziness in Protein Interactions—A Historical Perspective. J. Mol. Biol. 2018, 430, 2278–2287.
- (7) Mollica, L.; Bessa, L. M.; Hanoulle, X.; Jensen, M. R.; Blackledge, M.; Schneider, R. Binding mechanisms of intrinsically disordered proteins: theory, simulation, and experiment. *Frontiers in Molecular Biosciences* **2016**, *3*, 52.
- (8) Tompa, P.; Fuxreiter, M. Fuzzy complexes: polymorphism and structural disorder in protein-protein interactions. *Trends in biochemical sciences* **2008**, 33, 2–8.
- (9) Morris, O. M.; Torpey, J. H.; Isaacson, R. L. Intrinsically disordered proteins: modes of binding with emphasis on disordered domains. *Open Biology* **2021**, *11*, 210222.
- (10) Yang, J.; Gao, M.; Xiong, J.; Su, Z.; Huang, Y. Features of molecular recognition of intrinsically disordered proteins via coupled folding and binding. *Protein Sci.* **2019**, *28*, 1952–1965.
- (11) Bhattarai, A.; Emerson, I. A. Dynamic conformational flexibility and molecular interactions of intrinsically disordered proteins. *Journal of Biosciences* **2020**, *45*, 1–17.
- (12) Bugge, K.; Brakti, I.; Fernandes, C. B.; Dreier, J. E.; Lundsgaard, J. E.; Olsen, J. G.; Skriver, K.; Kragelund, B. B. Interactions by disorder—a matter of context. *Frontiers in Molecular Biosciences* **2020**, *7*, 110.
- (13) Toto, A.; Malagrino, F.; Visconti, L.; Troilo, F.; Pagano, L.; Brunori, M.; Jemth, P.; Gianni, S. Templated folding of intrinsically disordered proteins. *J. Biol. Chem.* **2020**, 295, 6586–6593.
- (14) Dyson, H. J.; Wright, P. E. Coupling of folding and binding for unstructured proteins. *Curr. Opin. Struct. Biol.* **2002**, *12*, 54–60.
- (15) Toto, A.; Troilo, F.; Visconti, L.; Malagrino, F.; Bignon, C.; Longhi, S.; Gianni, S. Binding induced folding: Lessons from the kinetics of interaction between NTAIL and XD. *Arch. Biochem. Biophys.* **2019**, *671*, 255–261.
- (16) Monod, J.; Wyman, J.; Changeux, J. P. On the nature of allosteric transitions: A plausible model. *J. Mol. Biol.* **1965**, *12*, 88–118.
- (17) Koshland, D. E. Application of a Theory of Enzyme Specificity to Protein Synthesis. *Proc. Natl. Acad. Sci. U. S. A.* **1958**, *44*, 98–104.
- (18) Ma, B.; Kumar, S.; Tsai, C.-J.; Nussinov, R. Folding funnels and binding mechanisms. *Protein engineering* **1999**, *12*, 713–720.
- (19) Levy, Y.; Cho, S. S.; Onuchic, J. N.; Wolynes, P. G. A survey of flexible protein binding mechanisms and their transition states using native topology based energy landscapes. *Journal of molecular biology* **2005**, 346, 1121–1145.
- (20) Tsai, C.-J.; Kumar, S.; Ma, B.; Nussinov, R. Folding funnels, binding funnels, and protein function. *Protein Sci.* **1999**, *8*, 1181–1190.
- (21) Hammes, G. G.; Chang, Y. C.; Oas, T. G. Conformational selection or induced fit: A flux description of reaction mechanism. *Proc. Natl. Acad. Sci. U.S.A.* **2009**, *106*, 13737–13741.
- (22) Shammas, S. L.; Crabtree, M. D.; Dahal, L.; Wicky, B. I.; Clarke, J. Insights into coupled folding and binding mechanisms from kinetic studies. *J. Biol. Chem.* **2016**, 291, 6689–6695.

- (23) Sugase, K.; Dyson, H. J.; Wright, P. E. Mechanism of coupled folding and binding of an intrinsically disordered protein. *Nature* **2007**, 447, 1021–1025.
- (24) Schneider, R.; Maurin, D.; Communie, G.; Kragelj, J.; Hansen, D. F.; Ruigrok, R. W.; Jensen, M. R.; Blackledge, M. Visualizing the molecular recognition trajectory of an intrinsically disordered protein using multinuclear relaxation dispersion NMR. *J. Am. Chem. Soc.* **2015**, 137, 1220–1229.
- (25) Malagrinò, F.; Diop, A.; Pagano, L.; Nardella, C.; Toto, A.; Gianni, S. Unveiling induced folding of intrinsically disordered proteins—Protein engineering, frustration and emerging themes. *Curr. Opin. Struct. Biol.* **2022**, *72*, 153–160.
- (26) Meir, A.; Macé, K.; Vegunta, Y.; Williams, S. M.; Waksman, G. Substrate recruitment mechanism by gram-negative type III, IV, and VI bacterial injectisomes. *Trends in Microbiology* **2023**, *31*, 916–932.
- (27) Souza, D. P.; Oka, G. U.; Alvarez-Martinez, C. E.; Bisson-Filho, A. W.; Dunger, G.; Hobeika, L.; Cavalcante, N. S.; Alegria, M. C.; Barbosa, L. R.; Salinas, R. K.; Guzzo, C. R.; Farah, C. S. Bacterial killing via a type IV secretion system. *Nat. Commun.* **2015**, *6*, 1–9.
- (28) Sgro, G. G.; Costa, T. R.; Cenens, W.; Souza, D. P.; Cassago, A.; Coutinho de Oliveira, L.; Salinas, R. K.; Portugal, R. V.; Farah, C. S.; Waksman, G. Cryo-EM structure of the bacteria-killing type IV secretion system core complex from Xanthomonas citri. *Nature Microbiology* **2018**, *3*, 1429–1440.
- (29) Oliveira, L. C.; Souza, D. P.; Oka, G. U.; Lima, F. d. S.; Oliveira, R. J.; Favaro, D. C.; Wienk, H.; Boelens, R.; Farah, C. S.; Salinas, R. K. VirB7 and VirB9 Interactions Are Required for the Assembly and Antibacterial Activity of a Type IV Secretion System. *Structure* **2016**, 24, 1707–1718.
- (30) Souza, D. P.; Andrade, M. O.; Alvarez-Martinez, C. E.; Arantes, G. M.; Farah, C. S.; Salinas, R. K. A component of the Xanthomonadaceae type IV secretion system combines a VirB7 motif with a N0 domain found in outer membrane transport proteins. *PLoS pathogens* **2011**, *7*, No. e1002031.
- (31) Saxena, V. P.; Wetlaufer, D. B. A new basis for interpreting the circular dichroic spectra of proteins. *Proc. Natl. Acad. Sci. U.S.A.* **1971**, 68, 969–972.
- (32) Woody, R. W. Aromatic side-chain contributions to the far ultraviolet circular dichroism of peptides and proteins. *Biopolymers* **1978**, *17*, 1451–1467.
- (33) Grishina, I. B.; Woody, R. W. Contributions of tryptophan side chains to the circular dichroism of globular proteins: Exciton couplets and coupled oscillators. *Faraday Discuss.* **1994**, *99*, 245–262.
- (34) Woody, R. W. Contributions of tryptophan side chains to the farultraviolet circular dichroism of proteins. *Eur. Biophys. J.* **1994**, 23, 253–262.
- (35) Miles, A. J.; Ramalli, S. G.; Wallace, B. A. DichroWeb, a website for calculating protein secondary structure from circular dichroism spectroscopic data. *Protein Sci.* **2022**, *31*, 37–46.
- (36) Semisotnov, G. V.; Rodionova, N. A.; Razgulyaev, O. I.; Uversky, V. N.; Gripas', A. F.; Gilmanshin, R. I. Study of the "molten globule" intermediate state in protein folding by a hydrophobic fluorescent probe. *Biopolymers* **1991**, *31*, 119–128.
- (37) Stryer, L. The interaction of a naphthalene dye with apomyoglobin and apohemoglobin: A fluorescent probe of non-polar binding sites. *J. Mol. Biol.* **1965**, *13*, 482–495.
- (38) Barone, G.; Catanzano, F.; Del Vecchio, P.; Giancola, C.; Graziano, G. Differential scanning calorimetry as a tool to study protein-ligand interactions. *Pure Appl. Chem.* **1995**, *67*, 1867–1872.
- (39) Hendrix, T.; Griko, Y. V.; Privalov, P. L. A calorimetric study of the influence of calcium on the stability of bovine  $\alpha$ -lactalbumin. *Biophys. Chem.* **2000**, *84*, 27–34.
- (40) González, M.; Argaraña, C. E.; Fidelio, G. D. Extremely high thermal stability of streptavidin and avidin upon biotin binding. *Biomolecular Engineering* **1999**, *16*, 67–72.
- (41) Johnson, C. M. Differential scanning calorimetry as a tool for protein folding and stability. *Arch. Biochem. Biophys.* **2013**, *531*, 100–109.

- (42) Celej, M. S.; Fidelio, G. D.; Dassie, S. A. Protein unfolding coupled to ligand binding: Differential scanning calorimetry simulation approach. *J. Chem. Educ.* **2005**, *82*, 85–92.
- (43) Pucci, F.; Rooman, M. Physical and molecular bases of protein thermal stability and cold adaptation. *Curr. Opin. Struct. Biol.* **2017**, 42, 117–128.
- (44) Layton, C. J.; Hellinga, H. W. Thermodynamic analysis of ligand-induced changes in protein thermal unfolding applied to high-throughput determination of ligand affinities with extrinsic fluorescent dyes. *Biochemistry* **2010**, *49*, 10831–10841.
- (45) Perozzo, R.; Folkers, G.; Scapozza, L. Thermodynamics of Protein Ligand Interactions: History, Presence, and Future Aspects. *Journal of receptors and signal transductions* **2004**, 24, 1–51.
- (46) Du, X.; Li, Y.; Xia, Y. L.; Ai, S. M.; Liang, J.; Sang, P.; Ji, X. L.; Liu, S. Q. Insights into protein—ligand interactions: Mechanisms, models, and methods. *International Journal of Molecular Sciences* **2016**, *17*, 144.
- (47) Spolar, R. S.; Record, M. T. Coupling of Local Folding to Site-Specific Binding of Proteins to DNA. *Science* **1994**, *263*, 777–784.
- (48) Vega, S.; Abian, O.; Velazquez-Campoy, A. On the link between conformational changes, ligand binding and heat capacity. *Biochimica et Biophysica Acta General Subjects* **2016**, *1860*, 868–878.
- (49) Schön, A.; Freire, E. Binding thermodynamics to intrinsically disordered protein domains. *Intrinsically Disordered Proteins: Methods and Protocols* **2020**, 2141, 449–462.
- (50) Shen, Y.; Delaglio, F.; Cornilescu, G.; Bax, A. TALOS+: A hybrid method for predicting protein backbone torsion angles from NMR chemical shifts. *Journal of Biomolecular NMR* **2009**, *44*, 213–223.
- (51) Tamiola, K.; Acar, B.; Mulder, F. A. Sequence-specific random coil chemical shifts of intrinsically disordered proteins. *J. Am. Chem. Soc.* **2010**, *132*, 18000–18003.
- (52) Shen, Y.; Bax, A. SPARTA+: A modest improvement in empirical NMR chemical shift prediction by means of an artificial neural network. *Journal of Biomolecular NMR* **2010**, *48*, 13–22.
- (53) Di Cera, E. Mechanisms of ligand binding. *Biophysics Reviews* **2020**, *1*, 011303.
- (54) Bagshaw, C. Biomolecular Kinetics: A Step-by-Step Guide; Foundations of Biochemistry and Biophysics; CRC Press, 2017; p 470.
- (55) Vogt, A. D.; Di Cera, E. Conformational selection or induced fit? A critical appraisal of the kinetic mechanism. *Biochemistry* **2012**, *51*, 5894–5902.
- (56) Gianni, S.; Dogan, J.; Jemth, P. Distinguishing induced fit from conformational selection. *Biophys. Chem.* **2014**, *189*, 33–39.
- (57) Floor, M.; Li, K.; Estévez-Gay, M.; Agulló, L.; Muñoz-Torres, P. M.; Hwang, J. K.; Osuna, S.; Villà-Freixa, J. SBMOpenMM: A Builder of Structure-Based Models for OpenMM. *J. Chem. Inf. Model.* **2021**, *61*, 3166–3171.
- (58) Kumar, S.; Rosenberg, J. M.; Bouzida, D.; Swendsen, R. H.; Kollman, P. A. THE weighted histogram analysis method for free-energy calculations on biomolecules. I. The method. *J. Comput. Chem.* **1992**, *13*, 1011–1021.
- (59) Wolynes, P. G.; Onuchic, J. N.; Thirumalai, D. Navigating the folding routes. *Science* **1995**, *267*, 1619–1620.
- (60) Chu, X.; Gan, L.; Wang, E.; Wang, J. Quantifying the topography of the intrinsic energy landscape of flexible biomolecular recognition. *Proc. Natl. Acad. Sci. U. S. A.* **2013**, *110*, E2342—E2351.
- (61) Freitas, F. C.; Ferreira, P. H. B.; Favaro, D. C.; Oliveira, R. J. d. Shedding light on the inhibitory mechanisms of SARS-CoV-1/CoV-2 spike proteins by ACE2-designed peptides. *J. Chem. Inf. Model.* **2021**, *61*, 1226–1243.
- (62) Vranken, W. F.; Boucher, W.; Stevens, T. J.; Fogh, R. H.; Pajon, A.; Llinas, M.; Ulrich, E. L.; Markley, J. L.; Ionides, J.; Laue, E. D. The CCPN data model for NMR spectroscopy: Development of a software pipeline. *Proteins: Struct., Funct., Bioinf.* **2005**, *59*, 687–696.
- (63) Delaglio, F.; Grzesiek, S.; Vuister, G. W.; Zhu, G.; Pfeifer, J.; Bax, A. NMRPipe: A multidimensional spectral processing system based on UNIX pipes. *Journal of Biomolecular NMR* **1995**, *6*, 277–293.
- (64) Cardoso, M. V.; Rivera, J. D.; Vitale, P. A.; Degenhardt, M. F.; Abiko, L. A.; Oliveira, C. L.; Salinas, R. K. CALX-CBD1 Ca2+-Binding

- Cooperativity Studied by NMR Spectroscopy and ITC with Bayesian Statistics. *Biophys. J.* **2020**, *119*, 337–348.
- (65) Farrow, N. A.; Zhang, O.; Forman-Kay, J. D.; Kay, L. E. A heteronuclear correlation experiment for simultaneous determination of 15 N longitudinal decay and chemical exchange rates of systems in slow equilibrium. *Journal of biomolecular NMR* **1994**, *4*, 727–734.
- (66) Whitmore, L.; Wallace, B. A. DICHROWEB, an online server for protein secondary structure analyses from circular dichroism spectroscopic data. *Nucleic Acids Res.* **2004**, 32, 668–673.
- (67) Whitmore, L.; Wallace, B. A. Protein secondary structure analyses from circular dichroism spectroscopy: Methods and reference databases. *Biopolymers* **2008**, *89*, 392–400.
- (68) Sreerama, N.; Woody, R. W. Estimation of protein secondary structure from circular dichroism spectra: comparison of CONTIN, SELCON, and CDSSTR methods with an expanded reference set. *Analytical biochemistry* **2000**, 287, 252–260.
- (69) Sjöstrand, L. Method Development for Thermal Stability Analysis by Circular Dichroism: Application to the Abp1p SH3 domain from yeast. *Bachelor's Thesis*, Linköping University, 2018.
- (70) Greenfield, N. J. Using circular dichroism collected as a function of temperature to determine the thermodynamics of protein unfolding and binding interactions. *Nat. Protoc.* **2006**, *1*, 2527–2535.
- (71) Seelig, J.; Schönfeld, H.-J. Thermal protein unfolding by differential scanning calorimetry and circular dichroism spectroscopy Two-state model versus sequential unfolding. Q. Rev. Biophys. 2016, 49, No. e9
- (72) Nakatani, H.; Haga, M.; Hiromi, K. Kinetic studies on binding of bovine serum albumin with 1-anilino-8-naphthalene sulfonate. *FEBS Lett.* **1974**, *43*, 293–296.
- (73) Yu, L.; Li, D.-W.; Brüschweiler, R. Balanced Amino-Acid-Specific Molecular Dynamics Force Field for the Realistic Simulation of Both Folded and Disordered Proteins. *J. Chem. Theory Comput.* **2020**, *16*, 1311–1318.
- (74) Van Der Spoel, D.; Lindahl, E.; Hess, B.; Groenhof, G.; Mark, A. E.; Berendsen, H. J. C. GROMACS: Fast, flexible, and free. *J. Comput. Chem.* **2005**, *26*, 1701–1718.
- (75) Søndergaard, C. R.; Olsson, M. H.; Rostkowski, M.; Jensen, J. H. Improved treatment of ligands and coupling effects in empirical calculation and rationalization of p K a values. *J. Chem. Theory Comput.* **2011**, *7*, 2284–2295.
- (76) Whitford, P. C.; Noel, J. K.; Gosavi, S.; Schug, A.; Sanbonmatsu, K. Y.; Onuchic, J. N. An all-atom structure-based potential for proteins: Bridging minimal models with all-atom empirical forcefields. *Proteins: Struct., Funct., Bioinf.* **2009**, *75*, 430–441.
- (77) Taketomi, H.; Ueda, Y.; Gō, N. Studies on protein folding, unfolding and fluctuations by computer simulation. *International Journal of Peptide and Protein Research* 1975, 7, 445–459.
- (78) Clementi, C.; Nymeyer, H.; Onuchic, J. N. Topological and energetic factors: What determines the structural details of the transition state ensemble and 'en-route' intermediates for protein folding? An investigation for small globular proteins. *J. Mol. Biol.* **2000**, 298, 937–953.
- (79) Wang, J.; Oliveira, R. J.; Chu, X.; Whitford, P. C.; Chahine, J.; Han, W.; Wang, E.; Onuchic, J. N.; Leite, V. B. Topography of funneled landscapes determines the thermodynamics and kinetics of protein folding. *Proc. Natl. Acad. Sci. U. S. A.* **2012**, *109*, 15763–15768.
- (80) Sutto, L.; Lätzer, J.; Hegler, J. A.; Ferreiro, D. U.; Wolynes, P. G. Consequences of localized frustration for the folding mechanism of the IM7 protein. *Proc. Natl. Acad. Sci. U. S. A.* **2007**, *104*, 19825–19830.
- (81) Contessoto, V. G.; Lima, D. T.; Oliveira, R. J.; Bruni, A. T.; Chahine, J.; Leite, V. B. Analyzing the effect of homogeneous frustration in protein folding. *Proteins: Struct., Funct., Bioinf.* **2013**, *81*, 1727–1737.
- (82) Ferreira, P. H. B.; Freitas, F. C.; McCully, M. E.; Slade, G. G.; de Oliveira, R. J. The role of electrostatics and folding kinetics on the thermostability of homologous cold shock proteins. *J. Chem. Inf. Model.* **2020**, *60*, 546–561.
- (83) Noel, J. K.; Levi, M.; Raghunathan, M.; Lammert, H.; Hayes, R. L.; Onuchic, J. N.; Whitford, P. C. SMOG 2: A Versatile Software

Package for Generating Structure-Based Models. PLOS Computational Biology 2016, 12, e1004794.

- (84) Ferrenberg, A. M.; Swendsen, R. H. New Monte Carlo Technique for Studying Phase Transitions. *Physical review letters* **1988**, *61*, 2635–2638.
- (85) Freitas, F. C.; Maldonado, M.; Oliveira Junior, A. B.; Onuchic, J. N.; Oliveira, R. J. d. Biotin-painted proteins have thermodynamic stability switched by kinetic folding routes. *J. Chem. Phys.* **2022**, *156*, 195101.
- (86) Humphrey, W.; Dalke, A.; Schulten, K. VMD: visual molecular dynamics. *J. Mol. Graphics* **1996**, *14*, 33–38.
- (87) Pettersen, E. F.; Goddard, T. D.; Huang, C. C.; Couch, G. S.; Greenblatt, D. M.; Meng, E. C.; Ferrin, T. E. UCSF Chimera—A visualization system for exploratory research and analysis. *J. Comput. Chem.* **2004**, *25*, 1605–1612.
- (88) Hunter, J. D. Matplotlib: A 2D graphics environment. *Computing in science & engineering* **2007**, *9*, 90–95.